

## Chapter 3

# Cosmic ray transport

### 3.1 Introduction

The heliosphere modulates the intensity of the galactic cosmic ray spectrum (traditionally expected at the heliopause) as these particles enter the heliosphere, changing the cosmic ray intensities as a function of time, position and energy. A recent study by *Scherer et al. (2011)* suggests there may even be modulation of cosmic rays beyond the heliopause, even up to the bow shock/wave, suggesting a difference between what can be called a heliopause spectrum and a local galactic or interstellar spectrum. However, this aspect is beyond the scope of this work and it is assumed that the heliopause is the modulation boundary where a heliopause spectrum is specified.

As shown in Chapter 2, cosmic ray modulation produces a  $\sim 11$  year cyclic variation of intensities as observed by neutron monitors at the surface of Earth and also by different spacecraft in the heliosphere. The level of cosmic ray modulation varies in anti-correlation with solar activity i.e. low cosmic ray intensities are observed during solar maximum periods and vice versa for solar minimum. Furthermore, cosmic ray modulation is also dependent on the energy of these particles.

The four major processes which modulate cosmic ray intensities in the heliosphere are:

1. Convection: Cosmic rays entering the heliosphere are convected out with the solar wind which blows radially outwards from the Sun (see *Parker, 1958, 1960*).
2. Energy changes: Cosmic rays are adiabatically cooled (decelerated) (e.g. *Parker, 1965*) or heated (accelerated) (see *Langner et al., 2006; Ferreira et al., 2007b*) as the plasma expand or being compressed. They may also be accelerated at the solar wind TS via diffusive shock acceleration (see *Bell, 1978a,b; Blandford and Ostriker, 1978; Pesses et al., 1981; Drury, 1983; Le Roux et al., 1996*) or continuous stochastic acceleration in the inner heliosheath (see *Axford, 1981; Moraal et al., 2006; Zhang, 2006; Ferreira et al., 2007b; Fisk and Gloeckler, 2009; Strauss et al., 2010b*).

3. Diffusion: Cosmic rays are diffused along the HMF (parallel) and across HMF lines (perpendicular) (e.g. *Bieber et al., 1994; Schlickeiser and Miller, 1998; Teufel and Schlickeiser, 2003; Shalchi et al., 2004; Engelbrecht, 2008*).
4. Drift: Cosmic rays drift due to the gradient and curvature of the HMF or due to changes in the magnetic field direction as in the HCS (see *Jokipii et al., 1977; Potgieter and Moraal, 1985; Hattingh and Burger, 1995b; Visser, 2010*).

In this chapter, the focus is on cosmic ray diffusion and drifts, where the corresponding spatial and energy dependence of these transport coefficients are discussed as they are implemented in the numerical model used in this work.

### 3.2 Parker transport equation

The above-mentioned modulation processes were combined by *Parker (1965)* into a transport equation (TPE) which was later re-derived by *Gleeson and Axford (1967)* and then refined by *Gleeson and Axford (1968)* and *Jokipii and Parker (1970)*. The TPE is given as,

$$\frac{\partial f}{\partial t} = -(\mathbf{V} + \langle \mathbf{v}_d \rangle) \cdot \nabla f + \nabla \cdot (\mathbf{K}_S \cdot \nabla f) + \frac{1}{3}(\nabla \cdot \mathbf{V}) \frac{\partial f}{\partial \ln P} + Q. \quad (3.1)$$

Here  $t$  is the time,  $P$  is rigidity,  $Q$  is any particle source inside the heliosphere,  $\mathbf{V}$  is the solar wind velocity,  $\mathbf{K}_S$  is the isotropic diffusion tensor and  $\langle \mathbf{v}_d \rangle$  the pitch angle averaged guiding center drift velocity (e.g. *Burger et al., 2000; Stawicki, 2005a*) for a near isotropic distribution function  $f$ . The differential intensity  $j$  is related to  $f$  by  $j = P^2 f$ . This equation is solved numerically in this work in terms of time and rigidity in two-dimensional space  $(r, \theta)$  with  $r$  the radial distance and  $\theta$  the polar angle. The rigidity  $P$  is defined as the momentum per charge for a given particle i.e  $P = \frac{pc}{q}$  with  $p$  the particle's momentum,  $q$  the charge and  $c$  the speed of light.

Equation 3.1 contains all the important cosmic ray modulation processes. The first term on the right hand side of the equation represents the outward convection due to the solar wind, the second term represents the drift effects due to the background magnetic field, the third term represents the spatial diffusion parallel and perpendicular to the background magnetic field, the fourth term represents the energy changes and the fifth term represents possible sources inside the heliosphere e.g. jovian electrons or anomalous cosmic rays as discussed in the previous chapter. The term on the left hand side represents the changes in cosmic ray distribution with time.

The TPE in a three-dimensional (3D) spherical coordinate system rotating with the Sun (as-

suming spherical symmetry) is given as

$$\begin{aligned}
 \frac{\partial f}{\partial t} = & \left[ \frac{1}{r^2} \frac{\partial}{\partial r} (r^2 K_{rr}) + \frac{1}{r \sin \theta} \frac{\partial}{\partial \theta} (K_{\theta r} \sin \theta) + \frac{1}{r \sin \theta} \frac{\partial K_{\phi r}}{\partial \phi} - V \right] \frac{\partial f}{\partial r} \\
 & + \left[ \frac{1}{r^2} \frac{\partial}{\partial r} (r K_{r\theta}) + \frac{1}{r^2 \sin \theta} \frac{\partial}{\partial \theta} (K_{\theta\theta} \sin \theta) + \frac{1}{r^2 \sin \theta} \frac{\partial K_{\phi\theta}}{\partial \phi} \right] \frac{\partial f}{\partial \theta} \\
 & + \left[ \frac{1}{r^2 \sin \theta} \frac{\partial}{\partial r} (r K_{r\phi}) + \frac{1}{r^2 \sin \theta} \frac{\partial K_{\theta\phi}}{\partial \theta} + \frac{1}{r^2 \sin^2 \theta} \frac{\partial K_{\phi\phi}}{\partial \phi} + \Omega \right] \frac{\partial f}{\partial \phi} \\
 & + K_{rr} \frac{\partial^2 f}{\partial r^2} + \frac{K_{\theta\theta}}{r^2} \frac{\partial^2 f}{\partial \theta^2} + \frac{K_{\phi\phi}}{r^2 \sin^2 \theta} \frac{\partial^2 f}{\partial \phi^2} + \frac{2K_{r\phi}}{r \sin \theta} \frac{\partial^2 f}{\partial r \partial \phi} \\
 & + \frac{1}{3r^2} \frac{\partial}{\partial r} (r^2 V) \frac{\partial f}{\partial \ln P} + Q,
 \end{aligned} \tag{3.2}$$

where  $K_{rr}$ ,  $K_{r\theta}$ ,  $K_{r\phi}$ ,  $K_{\theta r}$ ,  $K_{\theta\theta}$ ,  $K_{\theta\phi}$ ,  $K_{\phi r}$ ,  $K_{\phi\theta}$  and  $K_{\phi\phi}$  are the different elements in the diffusion tensor  $\mathbf{K}$  which will be discussed in section 3.3,  $\Omega$  the angular speed of the Sun and  $V$  the solar wind speed.

For a two-dimensional (2D) approach, as assumed in this work, an azimuthal symmetry is assumed in Equation 3.2 (i.e.  $\frac{\partial}{\partial \phi} = 0$ ) and the equation becomes

$$\begin{aligned}
 \frac{\partial f}{\partial t} = & \left[ \frac{1}{r^2} \frac{\partial}{\partial r} (r^2 K_{rr}) + \frac{1}{r \sin \theta} \frac{\partial}{\partial \theta} (K_{\theta r} \sin \theta) - V \right] \frac{\partial f}{\partial r} \\
 & + \left[ \frac{1}{r^2} \frac{\partial}{\partial r} (r K_{r\theta}) + \frac{1}{r^2 \sin \theta} \frac{\partial}{\partial \theta} (K_{\theta\theta} \sin \theta) \right] \frac{\partial f}{\partial \theta} \\
 & + K_{rr} \frac{\partial^2 f}{\partial r^2} + \frac{K_{\theta\theta}}{r^2} \frac{\partial^2 f}{\partial \theta^2} + \frac{1}{3r^2} \frac{\partial}{\partial r} (r^2 V) \frac{\partial f}{\partial \ln P} + Q.
 \end{aligned} \tag{3.3}$$

This 2D TPE (*Le Roux, 1990*) is solved numerically in this work to compute cosmic ray intensities inside the heliosphere, assuming no particle sources inside the heliosphere (i.e.  $Q = 0$ ). The different transport coefficients are discussed next.

### 3.3 Diffusion tensor

The symmetric diffusion tensor  $\mathbf{K}_s$  in Equation 3.1 in an average background HMF aligned coordinate system can be represented as

$$\mathbf{K}_s = \begin{bmatrix} K_{\parallel} & 0 & 0 \\ 0 & K_{\perp\theta} & 0 \\ 0 & 0 & K_{\perp r} \end{bmatrix}. \tag{3.4}$$

In Equation 3.4 (see e.g. *Effenberg et al., 2012*),  $K_{\parallel}$  is the diffusion coefficient parallel to the average HMF,  $K_{\perp\theta}$  the diffusion coefficient perpendicular to the average HMF in the  $\theta$  (polar) direction and  $K_{\perp r}$ , the diffusion coefficient perpendicular to the average HMF in the  $r$  (radial) direction. Figure 3.1 shows a graphical representation of the elements of  $\mathbf{K}_s$  with respect to a HMF  $\mathbf{B}$ . The direction along which  $K_{\parallel}$  acts is in or out of the page,  $K_{\perp\theta}$  towards the polar directions of the Sun and  $K_{\perp r}$  directed radially towards or away from the Sun. Also the average HMF  $\mathbf{B}$  is shown directed out of the page at a given position.

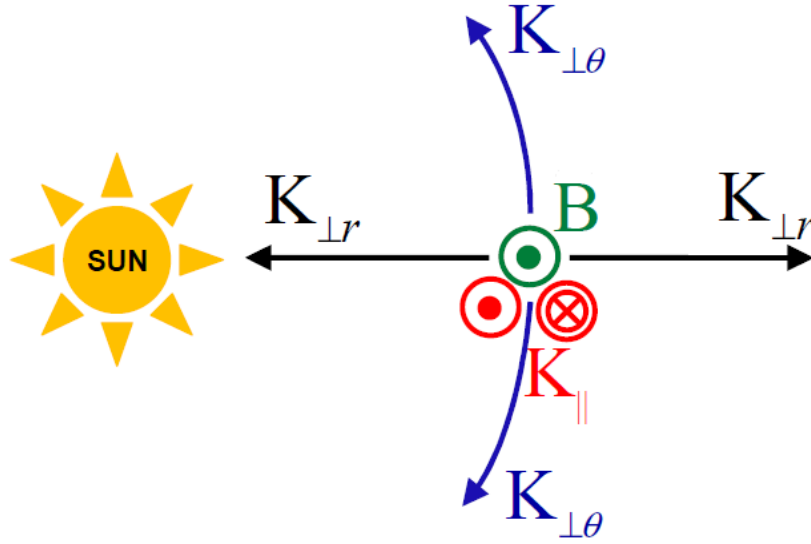


Figure 3.1: A graphical representation of the elements of  $\mathbf{K}_s$ , Equation 3.4.  $K_{||}$  is the diffusion coefficient parallel to the average HMF (into or out of the page),  $K_{\perp\theta}$  and  $K_{\perp r}$  are the diffusion coefficients perpendicular to the average HMF in the  $\theta$  (polar) direction and in the  $r$  (radial) direction respectively. Also shown is  $\mathbf{B}$  which represents the average HMF direction (out of the page) at a given position. Adapted from *Scherer et al. (2006b)*.

The asymmetric drift tensor  $\mathbf{K}_A$ , with  $K_A$  the drift coefficient, is

$$\mathbf{K}_A = \begin{bmatrix} 0 & 0 & 0 \\ 0 & 0 & K_A \\ 0 & -K_A & 0 \end{bmatrix}. \quad (3.5)$$

See Section 3.7 for a thorough discussion of the drift coefficient.

The full diffusion tensor  $\mathbf{K}$  in HMF aligned coordinates can be written as a sum of  $\mathbf{K}_s$ , the spatial diffusion tensor and  $\mathbf{K}_A$ , the drift tensor,

$$\mathbf{K} = \mathbf{K}_s + \mathbf{K}_A. \quad (3.6)$$

This results in

$$\mathbf{K} = \begin{bmatrix} K_{||} & 0 & 0 \\ 0 & K_{\perp\theta} & K_A \\ 0 & -K_A & K_{\perp r} \end{bmatrix}. \quad (3.7)$$

Using this tensor  $\mathbf{K}$ , Equation 3.1 can be rewritten as,

$$\frac{\partial f}{\partial t} = -\mathbf{V} \cdot \nabla f + \nabla \cdot (\mathbf{K} \cdot \nabla f) + \frac{1}{3}(\nabla \cdot \mathbf{V}) \frac{\partial f}{\partial \ln P} + Q. \quad (3.8)$$

To transform the field-aligned coordinates of  $\mathbf{K}$  to spherical coordinates, the spiral angle  $\psi$ , the angle between the radial and the average HMF direction at a given position, is used. The base

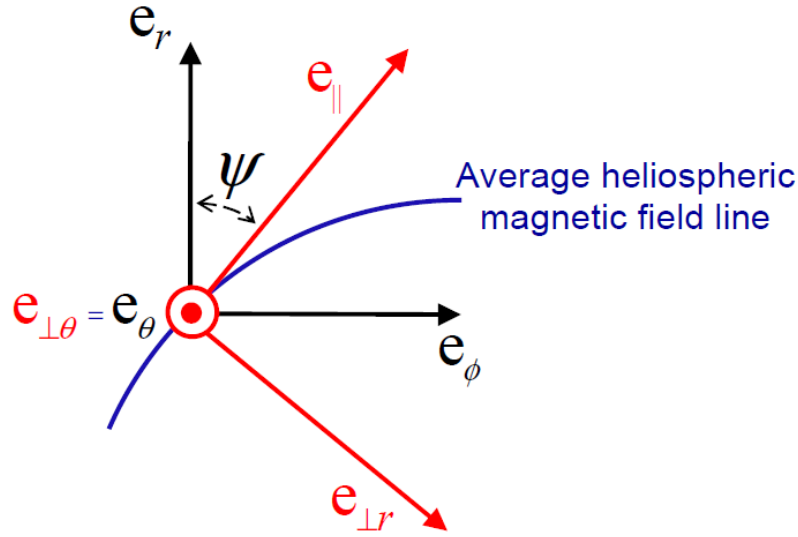


Figure 3.2: The base vector representations of the magnetic field aligned coordinate system and the spherical polar coordinate system. Here  $\mathbf{e}_{||}$  is the unit vector parallel to the average heliospheric magnetic field line (blue line),  $\mathbf{e}_{\perp\theta}$  the unit vector perpendicular to  $\mathbf{e}_{||}$  in the polar direction and  $\mathbf{e}_{\perp r}$  the unit vector perpendicular to  $\mathbf{e}_{||}$  in the radial direction, while  $\mathbf{e}_r$ ,  $\mathbf{e}_\theta$  and  $\mathbf{e}_\phi$  are the unit vectors in the spherical polar coordinate system. Also shown is the spiral angle  $\psi$ , the angle between  $\mathbf{e}_r$  and  $\mathbf{e}_{||}$ .

vectors for the field aligned coordinates are,

$$\begin{aligned} \mathbf{e}_{||} &= \cos \psi \mathbf{e}_r - \sin \psi \mathbf{e}_\phi \\ \mathbf{e}_{\perp\theta} &= \mathbf{e}_\theta \\ \mathbf{e}_{\perp r} &= \sin \psi \mathbf{e}_r + \cos \psi \mathbf{e}_\phi. \end{aligned} \quad (3.9)$$

Note that  $\mathbf{e}_{||} \times \mathbf{e}_{\perp\theta} = \mathbf{e}_{\perp r}$  to ensure a right-handed coordinate system. A graphical representation of the relation between the two coordinate systems (as discussed above) is shown in Figure 3.2. The figure shows the base vector representations of the magnetic field aligned coordinate system and the spherical polar coordinate system. Here  $\mathbf{e}_{||}$  is the unit vector parallel to the average heliospheric magnetic field line (blue line),  $\mathbf{e}_{\perp\theta}$  the unit vector perpendicular to  $\mathbf{e}_{||}$  in the polar direction and  $\mathbf{e}_{\perp r}$  the unit vector perpendicular to  $\mathbf{e}_{||}$  in radial direction, while  $\mathbf{e}_r$ ,  $\mathbf{e}_\theta$  and  $\mathbf{e}_\phi$  are the unit vectors in the spherical polar coordinate system. The figure also shows the spiral angle  $\psi$ , the angle between  $\mathbf{e}_r$  and  $\mathbf{e}_{||}$ .

The transformation matrix from spherical to field aligned coordinates is given as,

$$\begin{aligned} \mathbf{T}' &= \begin{bmatrix} \cos \psi & 0 & -\sin \psi \\ 0 & 1 & 0 \\ \sin \psi & 0 & \cos \psi \end{bmatrix} = \mathbf{T}^T \\ &= \mathbf{T}^{-1}. \end{aligned} \quad (3.10)$$

Here, superscript T denotes the transpose of the matrix. The inverse of the matrix is also the transpose since the matrix is orthogonal. The inverse of the above matrix, given in Equation

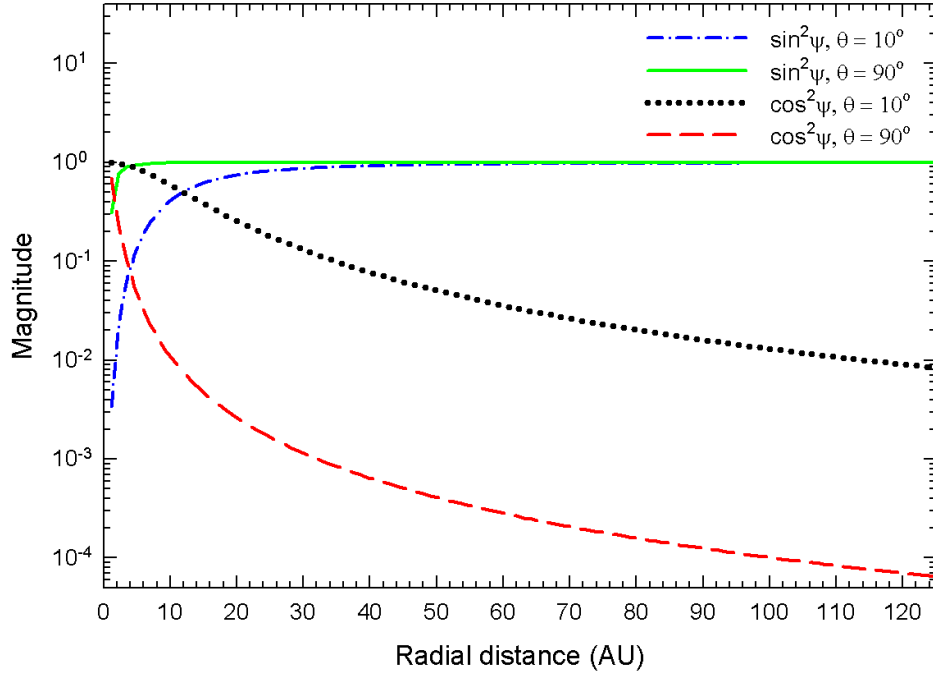


Figure 3.3: Shown here are the magnitude of  $\cos^2 \psi$  and  $\sin^2 \psi$  in Equation 3.13 as a function of radial distance for polar angles  $\theta = 10^\circ$  (polar regions) and  $\theta = 90^\circ$  (equatorial plane).

3.10, is the transformation matrix from field aligned coordinates to spherical coordinates and is given by

$$\mathbf{T} = \begin{bmatrix} \cos \psi & 0 & \sin \psi \\ 0 & 1 & 0 \\ -\sin \psi & 0 & \cos \psi \end{bmatrix}. \quad (3.11)$$

Therefore the diffusion tensor can be represented in spherical coordinates as,

$$\begin{aligned} \mathbf{K}' &= \begin{bmatrix} K_{rr} & K_{r\theta} & K_{r\phi} \\ K_{\theta r} & K_{\theta\theta} & K_{\theta\phi} \\ K_{\phi r} & K_{\phi\theta} & K_{\phi\phi} \end{bmatrix} \\ &= \mathbf{T} \mathbf{K} \mathbf{T}^\top \\ &= \begin{bmatrix} \cos \psi & 0 & \sin \psi \\ 0 & 1 & 0 \\ -\sin \psi & 0 & \cos \psi \end{bmatrix} \begin{bmatrix} K_{||} & 0 & 0 \\ 0 & K_{\perp\theta} & K_A \\ 0 & -K_A & K_{\perp r} \end{bmatrix} \begin{bmatrix} \cos \psi & 0 & -\sin \psi \\ 0 & 1 & 0 \\ \sin \psi & 0 & \cos \psi \end{bmatrix} \\ &= \begin{bmatrix} K_{||} \cos^2 \psi + K_{\perp r} \sin^2 \psi & -K_A \sin \psi & (K_{\perp r} - K_{||}) \cos \psi \sin \psi \\ K_A \sin \psi & K_{\perp\theta} & K_A \cos \psi \\ (K_{\perp r} - K_{||}) \cos \psi \sin \psi & -K_A \cos \psi & K_{||} \sin^2 \psi + K_{\perp r} \cos^2 \psi \end{bmatrix}. \end{aligned} \quad (3.12)$$

Two diffusion coefficients of particular concern for this study, which utilises a modulation

model in a spatial 2D-space ( $r$  and  $\theta$ ), are  $K_{rr}$  and  $K_{\theta\theta}$  and are given by,

$$\begin{aligned} K_{rr} &= K_{||} \cos^2 \psi + K_{\perp r} \sin^2 \psi \\ K_{\theta\theta} &= K_{\perp \theta}. \end{aligned} \quad (3.13)$$

Figure 3.3 shows  $\cos^2 \psi$  and  $\sin^2 \psi$  as a function of radial distance for values of polar angle  $\theta = 10^\circ$  and  $\theta = 90^\circ$  respectively. Shown in the figure is that the magnitude of  $\cos^2 \psi$  decreases from a maximum value 1 with increasing radial distance, while the magnitude of  $\sin^2 \psi$  increases with radial distance to reach a maximum value of 1 and thereafter stays constant throughout the outer heliosphere. In the inner heliosphere the magnitude of  $\cos^2 \psi$  is larger than  $\sin^2 \psi$  which results in  $K_{rr}$  being dominated by  $K_{||}$  while in the outer heliosphere the magnitude of  $\sin^2 \psi$  is considerably larger than  $\cos^2 \psi$  and results in a  $K_{\perp r}$  dominated  $K_{rr}$ . The figure also shows a latitude dependence of  $\cos^2 \psi$  and  $\sin^2 \psi$ . At the equatorial region ( $\theta = 90^\circ$ ) a steeper decrease in the magnitude of  $\cos^2 \psi$  is found when compared to the near polar region ( $\theta = 10^\circ$ ). However, for  $\sin^2 \psi$  a steeper increase in magnitude is found at the equatorial region when compared to the near polar region.

Next, the different transport coefficients ( $K_{||}$ ,  $K_{\perp r}$  and  $K_{\perp \theta}$ ) and how they couple to the background plasma and magnetic field are discussed. However, to appreciate this, some background on turbulence is first given.

### 3.4 Turbulence

Turbulence is regarded as a result of some random fluctuations in certain physical processes and is irregular in both space and time. An external force or addition of energy is required to sustain it against dissipation, without which it will eventually decay (see e.g. *Hinze, 1975; Falkovich and Sreenivasan, 2006*). The heliosphere is filled with the magnetised, supersonically expanding solar wind, which is highly fluctuating and turbulent (see e.g. *Erdos, 2003; Erdos and Balogh, 2005; Marino et al., 2009*). Cosmic ray transport in the heliosphere cannot be explained without including magnetic field fluctuations in the solar wind plasma. Cosmic ray diffusion is directly related to the structure of the HMF and the scattering of cosmic rays as a result of fluctuations in this field (see e.g. *Zank et al., 1996a; Burger et al., 2000; Teufel and Schlickeiser, 2002; Shalchi et al., 2004; Bruno and Carbone, 2005*).

#### 3.4.1 Turbulence power spectrum

The random fluctuations in the solar wind transform a wave packet with a certain wavelength to a shorter or longer wavelength. However, there is also a chance for a wave to decay to a shorter wavelength. This trend forms a cascade process in which the energy of fluctuations flows from long wavelengths (smaller wave numbers) to short wavelengths (larger wave numbers). From the spectrum of fluctuations, called the turbulence power spectrum (see *Bieber*

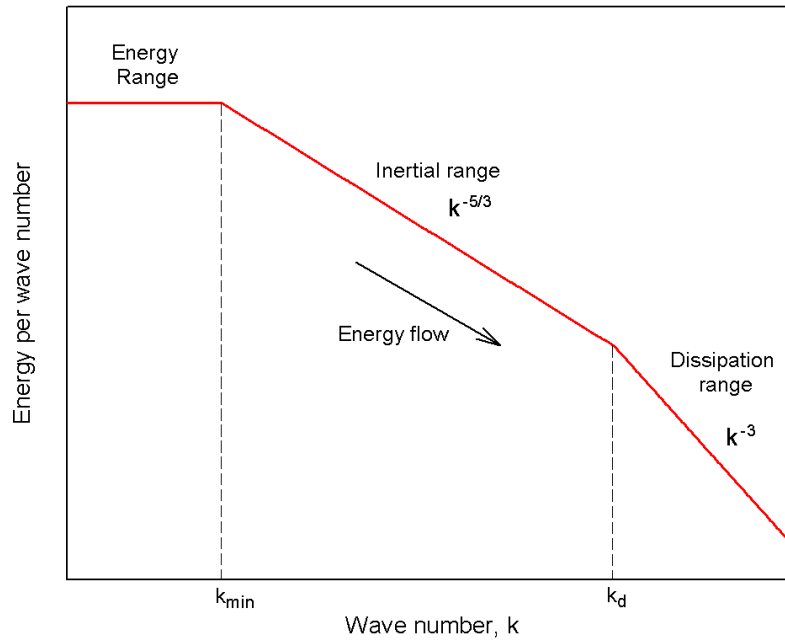


Figure 3.4: A schematic representation of a turbulence power spectrum (Bieber *et al.*, 1994; Goldstein *et al.*, 1995; Teufel and Schlickeiser, 2003). The power spectrum can be divided into three regions, namely the energy range which here is independent of the wave number ( $k$ ), the inertial range, where it is proportional to  $k^{-5/3}$  and the dissipation range where it is proportional to  $k^{-3}$ . The dotted vertical lines represents  $k_{min}$  the spectral break point between the inertial and energy range and  $k_d$  the spectral break point between inertial and dissipation range.

*et al.*, 1994; Goldstein *et al.*, 1995; Choudhuri, 1998; Teufel and Schlickeiser, 2003; Matthaeus *et al.*, 2007), three regions can be identified namely the energy range, inertial range and the dissipation range.

Figure 3.4 shows a schematic representation of a power spectrum of magnetic fluctuations or fluctuations of the total energy of solar wind. The energy range in the figure shows the region where the energy in fluctuations per wave number is traditionally assumed as independent of the wave number  $k$  (Bieber *et al.*, 1994; Goldstein *et al.*, 1995; Teufel and Schlickeiser, 2003). This region is not yet clearly understood and it is still under debate with suggestions that the energy in fluctuations per wave number in this range could also be proportional to  $k^{-1}$  (Bruno and Carbone, 2005; Shalchi, 2009). The middle region is inertial range where the energy is just transferred from low wave numbers to high wave numbers without being generated or consumed (Erdos, 2003). In this region the energy in fluctuations per wave number as predicted by Kolmogorov (1941) is proportional to  $k^{-5/3}$ , representing what is called a Kolmogorov cascade. Later, for a magnetohydrodynamics (MHD) case, Kraichnan (1965) introduced a spectrum with a spectral index  $-3/2$ , where the small scale fluctuations are influenced by the large scale magnetic field and the correlation between the velocity and magnetic field is weak. The inertial range spectra of the magnetic fluctuations measured at several spacecraft (e.g. Voyager, Helios, Mariner 10, Ulysses) in the solar wind support the Kolmogorov spectrum (Goldstein *et al.*, 1995;



*Horbury and Balogh, 2001; Erdos and Balogh, 2005; Bruno and Carbone, 2005*). Recently authors like *Horbury et al. (2008); Podesta (2009)* and *Luo and Wu (2010)* examined inertial range spectra using magnetic field data from Ulysses and both STEREO spacecraft and found that when the local mean magnetic field direction is anti-parallel (towards the Sun) or parallel (away from the Sun) to the solar wind flow, the spectral index decreases from -1.6 and it approaches -2 (see e.g. *Forman et al., 2011*).

The third region is the dissipation range where the cascade is terminated. Here the energy per wave number decreases more rapidly than in the inertial range and the energy is converted into heat which in turn leads to significant heating of background plasma (e.g. solar wind) (see e.g. *Leamon, 1999; Leamon et al., 2000; Erdos and Balogh, 2005; Smith et al., 2007*). In this region, the energy in fluctuations per wave number is proportional to  $k^{-3}$  according to *Bieber et al. (1994)*. A varying spectral index from -2 to -4 is also suggested by several authors (see e.g. *Leamon et al., 1998; Smith et al., 2006a; Howes et al., 2007*).

The spectral break between the energy range and the inertial range is represented as  $k_{min}$  and the spectral break between the inertial and dissipation range is represented as  $k_d$  (see e.g. *Bieber et al., 1994; Goldstein et al., 1995; Teufel and Schlickeiser, 2003*). The power spectrum of solar wind fluctuations is not solely a function of wavenumber but it also depends on heliocentric distance  $r$  (see review by *Bruno and Carbone, 2005*). *Horbury et al. (1996)* and *Engelbrecht (2008)* showed that  $k_{min}$  and  $k_d$  moves to a lower wave number as the plasma travels to larger distances from the Sun. Later, *Perri et al. (2010)* showed that using Ulysses and MESSENGER spacecraft solar wind data, that while  $k_{min}$  depends on radial distance from the Sun  $k_d$  is independent of distance from the Sun.

### 3.4.2 Turbulence models

A turbulent total magnetic field  $\mathbf{B}$  can be represented by means of a uniform mean background magnetic field with magnitude  $B_0$  and directed along the  $z$ -axis of a Cartesian coordinate system and a fluctuating component  $\delta\mathbf{B}$  as,

$$\mathbf{B} = B_0\mathbf{e}_z + \delta\mathbf{B}(x, y, z) \quad (3.14)$$

where the mean fluctuation  $\langle\delta\mathbf{B}\rangle = 0$ , i.e.  $\langle\mathbf{B}\rangle = B_0\mathbf{e}_z$ . The root mean square amplitude of  $\delta\mathbf{B}$  in the present study is denoted as  $\delta B$ , while  $\delta B^2$  represents the total energy in these fluctuations known as the magnetic field variance.

According to the turbulence geometry, turbulence can be represented by three models namely slab or one-dimensional (1D) turbulence, two-dimensional (2D) turbulence and the composite (or two-component) turbulence. In slab turbulence the magnitude of fluctuations  $\delta B_{slab}(z)$  are only a function of  $z$  along the mean magnetic field and are independent of the  $(x, y)$  coordinates.

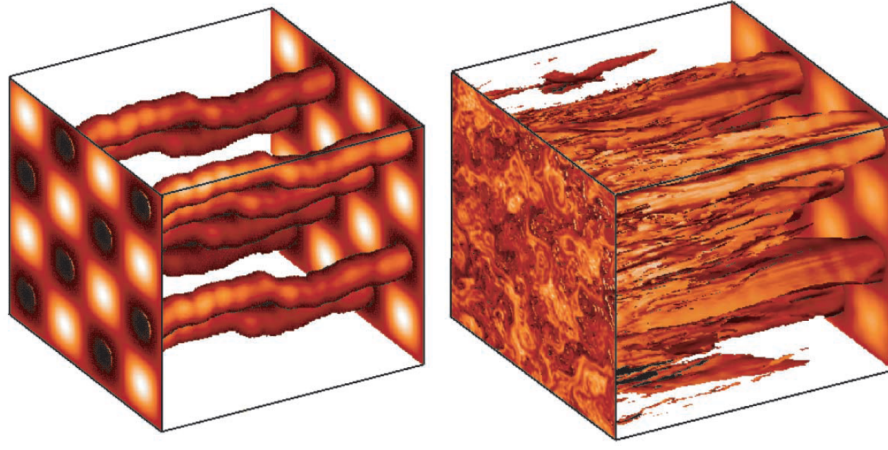


Figure 3.5: Magnetic flux tubes for two turbulent magnetic field models. Left panel: Pure slab turbulence with no transverse structure. The magnetic field lines shift in space while retaining their position and magnitude relative to one another. Right panel: Composite turbulence with 80 % of its energy in 2D mode and 20 % slab mode, exhibiting considerable transverse complexity leading to braiding and shredding of the field lines. From *Matthaeus et al. (2003)*.

The left panel of Figure 3.5 (from *Matthaeus et al., 2003*) shows a graphical representation of pure slab turbulence geometry where the magnitude of fluctuations are identical along all magnetic field lines for the same  $z$  coordinate. The slab turbulence generate synchronised fluctuations in each magnetic field line keeping their position and magnitude relative to one another. The turbulent total magnetic field in a slab geometry can be represented as,

$$\begin{aligned} \mathbf{B} &= B_0 \mathbf{e}_z + \delta \mathbf{B}_{slab}(z) \\ &= B_0 \mathbf{e}_z + \delta B_{slab,x}(z) \mathbf{e}_x + \delta B_{slab,y}(z) \mathbf{e}_y, \end{aligned} \quad (3.15)$$

and the slab variance is given by

$$\delta B_{slab}^2 = \delta B_{slab,x}^2 + \delta B_{slab,y}^2.$$

For turbulence that is axisymmetric with respect to mean magnetic field direction  $z$ , the  $x$  and  $y$  components of fluctuations are identical i.e.  $\delta B_{slab,x}(z) = \delta B_{slab,y}(z)$ , therefore,

$$\delta B_{slab}^2 = 2\delta B_{slab,x}^2 = 2\delta B_{slab,y}^2.$$

In 2D turbulence, fluctuations are assumed to reside in planes orthogonal to the mean magnetic field. The magnitude of fluctuations  $\delta B_{2D}(x, y)$  in 2D turbulence are independent of the coordinate  $z$  along the mean magnetic field. This leads to braiding and shredding of the magnetic flux tubes and hence different flux tubes starting at different  $(x, y)$  positions would not be similar, as in the case of slab turbulence. The turbulent total magnetic field in a purely 2D geometry can be represented as,

$$\begin{aligned} \mathbf{B} &= B_0 \mathbf{e}_z + \delta \mathbf{B}_{2D}(x, y) \\ &= B_0 \mathbf{e}_z + \delta B_{2D,x}(x, y) \mathbf{e}_x + \delta B_{2D,y}(x, y) \mathbf{e}_y, \end{aligned} \quad (3.16)$$

and the 2D variance is given by,

$$\delta B_{2D}^2 = \delta B_{2D,x}^2 + \delta B_{2D,y}^2.$$

Again for turbulence that is axisymmetric with respect to mean magnetic field direction i.e.  $\delta B_{2D,x}(x, y) = \delta B_{2D,y}(x, y)$  leads to,

$$\delta B_{2D}^2 = 2\delta B_{2D,x}^2 = 2\delta B_{2D,y}^2.$$

Theory and observations (e.g. *Matthaeus et al., 1990; Bieber et al., 1996; Matthaeus et al., 2007*) suggest a composite turbulence model with a 70%-90% of turbulent inertial energy range as 2D in the magnetic field fluctuations and remaining as slab. It is commonly assumed that 80% of the fluctuating inertial range energy as 2D and remaining 20% as slab, which is considered as a realistic scenario in the solar wind at 1 AU heliocentric distance (*Bieber et al., 1996; Giacalone and Jokipii, 1999; Shalchi, 2009*).

The right panel of Figure 3.5 shows the composite turbulence model where the magnetic field lines are braided and shredded due to the dominant 2D turbulence in the model. The amplitude of the fluctuations can be represented as,

$$\delta B = \sqrt{\delta B_{slab}^2 + \delta B_{2D}^2}.$$

Assuming an axisymmetric turbulence,

$$\delta B^2 = 2\delta B_{slab,x}^2(z) + 2\delta B_{2D,x}^2(x, y).$$

When a 20/80 ratio of slab to 2D variance is assumed throughout the heliosphere,

$$\delta B_{slab}^2 = 0.2\delta B^2,$$

and

$$\delta B_{2D}^2 = 0.8\delta B^2.$$

These variances (especially the time-dependence therein) are important for this study because it will be shown later how the different diffusion parameters depend on these.

### 3.5 Parallel diffusion coefficient

The parallel diffusion coefficient  $K_{||}$  describes cosmic ray diffusion along the average HMF. Parallel diffusion is mainly due to pitch angle scattering by the turbulent HMF. Figure 3.6 shows a graphical illustration of parallel diffusion experienced by a charged particle scattering in a turbulent magnetic field due to changes in the particle's pitch angle. The pitch angle is the angle between the particle's velocity vector and the magnetic field direction.  $K_{||}$  can be expressed in terms of the parallel mean free path  $\lambda_{||}$  and particle speed  $v$  as

$$K_{||} = \frac{v\lambda_{||}}{3}. \quad (3.17)$$

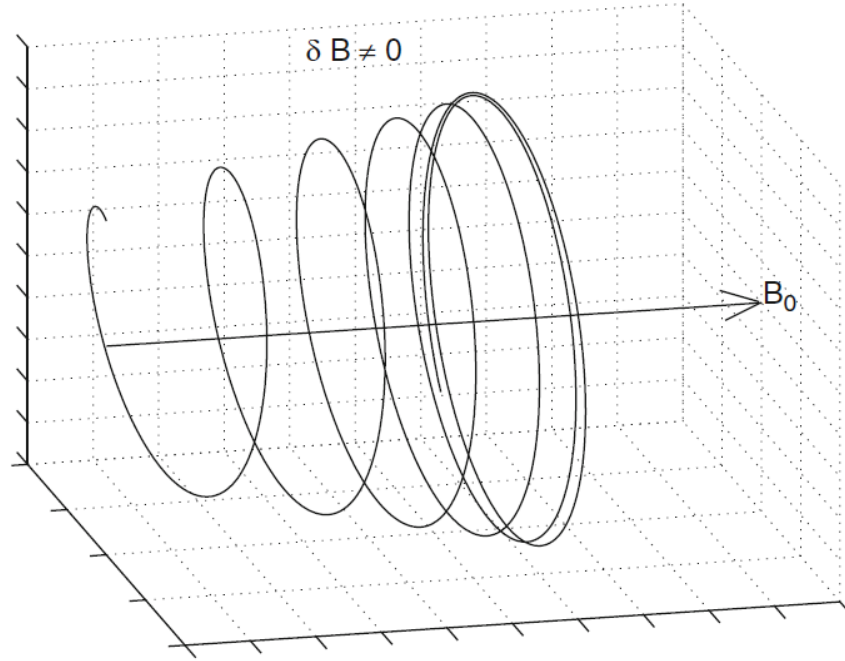


Figure 3.6: A graphical illustration of parallel diffusion experienced by a charged particle scattering in a turbulent magnetic field due to changes in the particle's pitch angle. For example, as a result of pitch angle scattering at  $90^\circ$  the particle can be scattered back to its initial position. From *Shalchi (2009)*.

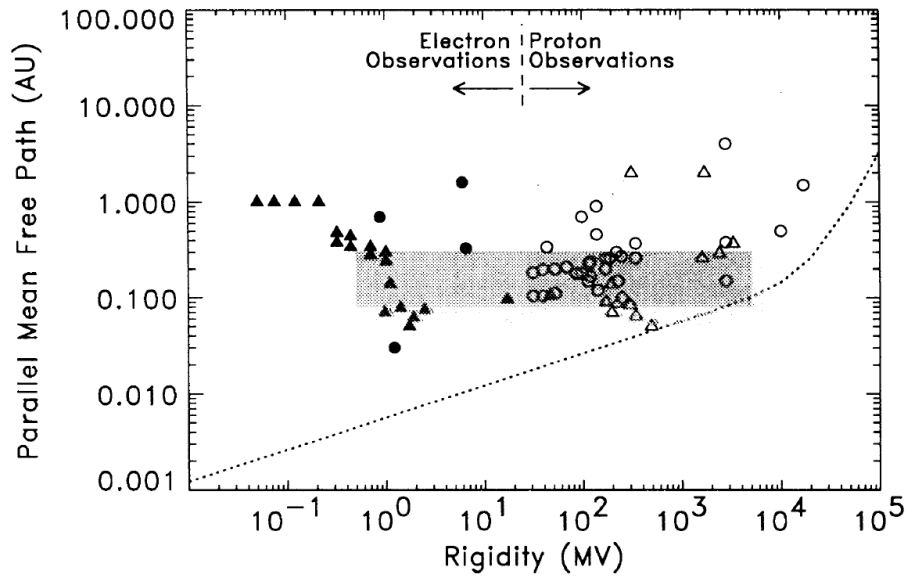


Figure 3.7: Cosmic ray parallel mean free path  $\lambda_{||}$  as a function of rigidity. Filled and open symbols denote results derived from electron and proton observations respectively. The shaded area represents the observational consensus of *Palmer (1982)*. The dotted line represents the prediction of standard quasi-linear theory for magnetostatic, dissipationless turbulence with purely slab geometry. From *Bieber et al. (1994)*.

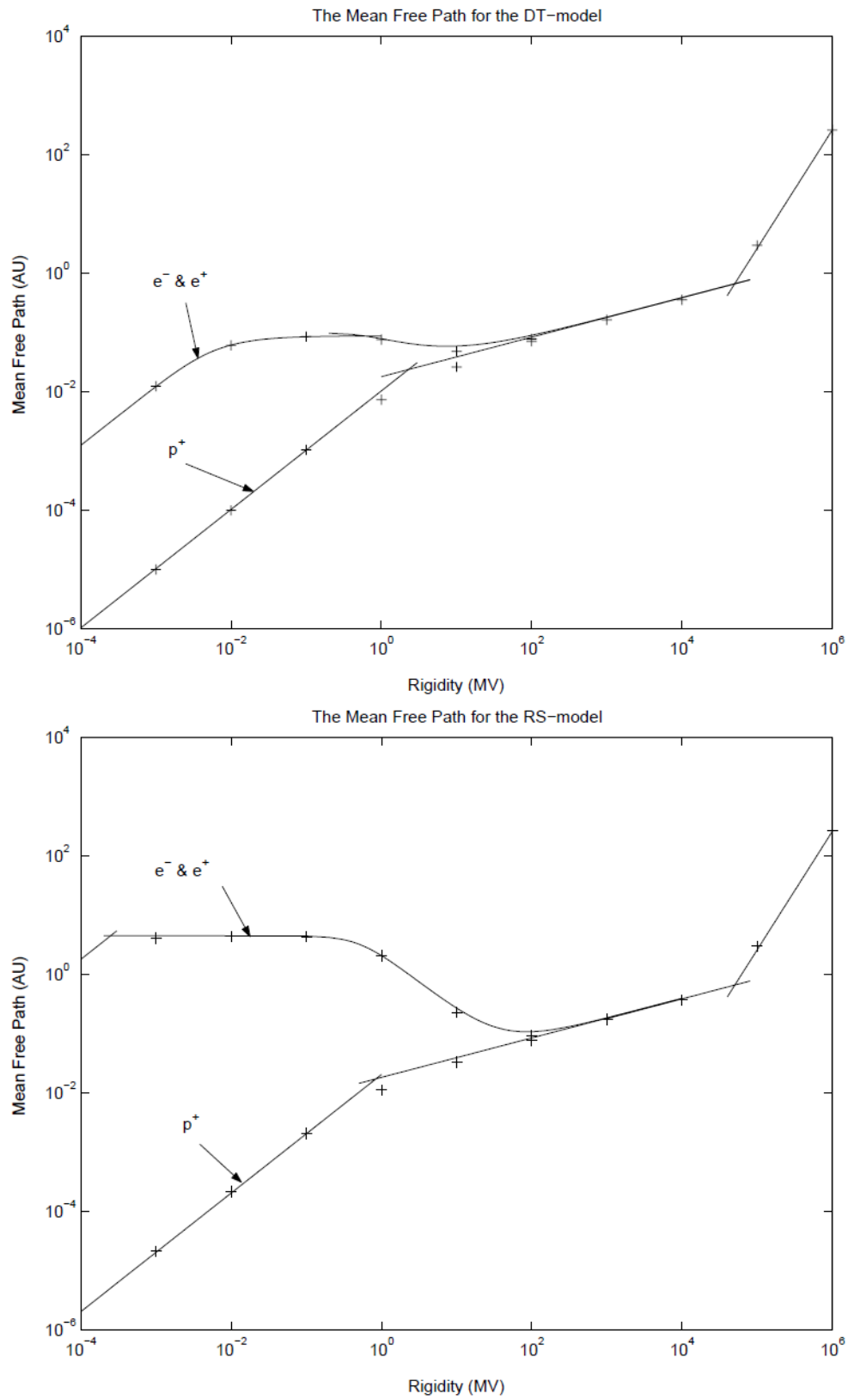


Figure 3.8: The top panel shows the parallel mean free paths at Earth for electrons ( $e^-$ ), positrons ( $e^+$ ) and protons ( $p^+$ ) for the damping model (DT) of dynamical turbulence and bottom panel shows the same but for the random sweeping model (RS). The crosses are the numerical results and the lines are the approximations. From *Teufel and Schlickeiser (2003)*.

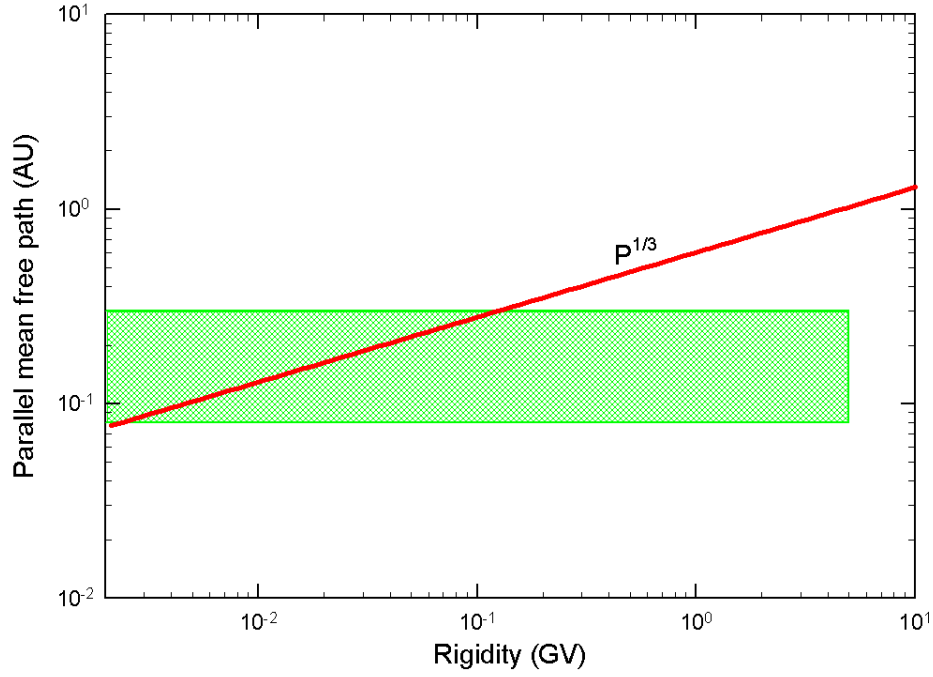


Figure 3.9: The proton parallel mean free path  $\lambda_{||}$ , at Earth as a function of rigidity. The shaded box represents the Palmer consensus (*Palmer, 1982*).

According to the quasi linear theory (QLT) (*Jokipii, 1966; Hasselmann and Wibberenz, 1970; Earl, 1974; Teufel and Schlickeiser, 2002*), the pitch angle averaged parallel mean free path is related to the pitch angle Fokker-Plank coefficient  $D_{\mu\mu}$  as,

$$\lambda_{||} = \frac{3v}{8} \int_{-1}^1 \frac{(1 - \mu^2)^2}{D_{\mu\mu}(\mu)} d\mu. \quad (3.18)$$

Here  $\mu$  is the cosine of the particle's pitch angle and can be represented as  $\mu = \frac{v_{||}}{v}$ , where  $v_{||}$  is a component of  $v$  parallel to the magnetic field direction.  $D_{\mu\mu}$  is calculated using the power spectrum of the magnetic field fluctuations as shown in Figure 3.4, Section 3.4.

### 3.5.1 Rigidity dependence

*Palmer (1982)* and later *Bieber et al. (1994)* compared the theoretical  $\lambda_{||}$  (Equation 3.18), predicted by Standard QLT (which used a magnetostatic slab model for the turbulence and the neglected dissipation range) with the solar particle observations and noticed that the theoretical  $\lambda_{||}$  is much smaller than the observations for smaller rigidity values. This problem of small  $\lambda_{||}$  predicted by QLT, when compared to observations, is coined by *Bieber et al. (1994)* as the “magnitude problem”. This is shown in Figure 3.7 with filled and open symbols representing results derived from electron and proton observations and the dotted line representing the predicted  $\lambda_{||}$  by QLT.

The theoretical  $\lambda_{||}$  decreases with decreasing rigidity whereas the observations generally stay-

ed constant for rigidities in the range 0.5 MV to 5000 MV implying no rigidity dependence for  $\lambda_{||}$ . *Bieber et al. (1994)* also named this second problem as the “flatness problem”. The shaded area shows the Palmer consensus values (*Palmer, 1982*), which shows the range of parallel mean free path for rigidities between 0.5 MV and 5000 MV, as 0.08 AU to 0.3 AU. These consensus values of the mean free paths near 1 AU was found by *Palmer (1982)* after analysing the intensity time profiles in solar cosmic ray events.

As mentioned above, by neglecting the dissipation range of the power spectrum and using the magnetostatic slab model during the above stated theoretical  $\lambda_{||}$  prediction, resulted in a very small  $\lambda_{||}$  for low rigidities and also an incorrect rigidity dependence (*Bieber et al., 1994*). During resonant scattering of low energy particles where the pitch angle reach  $90^\circ$ , the dissipation range is significant (*Smith et al., 1990*). The magnetometer and plasma wave observations (see *Coroniti et al., 1982*) show that magnetic turbulence spectra do exhibit a dissipation range. However, for low energy proton modulation in the heliosphere the  $\lambda_{||}$  (derived without the dissipation range) is applicable because the cosmic ray protons undergoes significant adiabatic energy changes below  $\sim 300$  MeV. The proton modulation appears unaffected by  $\lambda_{||}$  variations for these lower energies (see *Potgieter, 1996; Potgieter and Ferreira, 1999; Ferreira, 2002*). Note that this is not the case for electrons.

When the dissipation range (steep wave spectra with spectral index -3) was introduced to Equation 3.18, the  $\lambda_{||}$  was calculated to be infinity (*Bieber et al., 1994; Shalchi, 2005b*). This was due to the fact that the  $D_{\mu\mu}$  quickly tends to zero as pitch angle approaches  $90^\circ$  when compared to the case without dissipation range. To overcome this, various techniques were proposed by different authors, e.g. “mirroring” by fluctuations of the magnetic field magnitude (*Goldstein et al., 1975*), strong turbulence, weak coupling theory (*Goldstein, 1976*), dynamical turbulence (*Bieber and Matthaeus, 1991; Bieber et al., 1994*) and second-order QLT by calculating second-order pitch angle Fokker-Plank coefficient (*Shalchi, 2005b; Tautz et al., 2008*).

The introduction of the effect of dynamical turbulence model by *Bieber and Matthaeus (1991)* and *Bieber et al. (1994)* which solved the flatness problem of electrons is considered as an acceptable approach which caused  $D_{\mu\mu}$  not to approach zero for small  $\mu$  for lower rigidities (see *Hattingh, 1998*). However, Equation 3.18 can only be solved numerically after incorporating the dissipation range and composite turbulence (geometry other than pure slab model solved the magnitude problem), due to its complexity. *Bieber et al. (1994)* included the effects of dynamical turbulence by defining two models namely the damping model and the random sweeping model.

Utilising the set of parameters suggested by *Bieber et al. (1994)*, which are appropriate for interplanetary conditions, *Teufel and Schlickeiser (2003)* predicted a  $\lambda_{||}$  at Earth using damping (DT) and random sweeping (RS) models as shown in Figure 3.8. The top panel of the figure shows the  $\lambda_{||}$  at Earth for electrons ( $e^-$ ), positrons ( $e^+$ ) and protons ( $p^+$ ) for the DT model and the bottom panel shows the same but for the RS model. The crosses in the figure represents the numerical solutions of  $\lambda_{||}$  and the lines are their piecewise continuous analytical approxima-



tions.

The analytical approximations of  $\lambda_{||}$  (in AU) at Earth as given by *Teufel and Schlickeiser (2003)* using the DT model for protons for three different rigidity ranges are:

$$\begin{aligned}\lambda_{||} &\propto \left(\frac{P}{P_0}\right)^2 \quad \text{for } P > 10^4 \text{ MV}, \\ \lambda_{||} &\propto \left(\frac{P}{P_0}\right)^{\frac{1}{3}} \quad \text{for } 10^{-1} \text{ MV} \leq P \leq 10^4 \text{ MV}, \\ \lambda_{||} &\propto \left(\frac{P}{P_0}\right) \quad \text{for } P < 10^{-1} \text{ MV},\end{aligned}\tag{3.19}$$

where  $P_0 = 1 \text{ MV}$ . The  $\lambda_{||}$  for electrons and positrons using the DT model is given as

$$\begin{aligned}\lambda_{||} &\propto \left(\frac{P}{P_0}\right)^2 \quad \text{for } P > 10^4 \text{ MV}, \\ \lambda_{||} &\propto \left[ \left(\frac{P}{P_0}\right)^{\frac{1}{3}} + \frac{3.57}{\left(\left(\frac{P_e}{P_0}\right)^2 + \left(\frac{P}{P_0}\right)^2\right)^{\frac{1}{4}}} \right] \quad \text{for } 10^{-1} \text{ MV} \leq P \leq 10^4 \text{ MV}, \\ \lambda_{||} &\propto \left[ \frac{P_1}{P} \left(1 + \left(\frac{P_1}{P}\right)^2\right) \arctan\left(\frac{P}{P_1}\right) \right] \quad \text{for } P < 10^{-1} \text{ MV},\end{aligned}\tag{3.20}$$

where  $P_e = 0.511 \text{ MV}$  and  $P_1 = 0.003 \text{ MV}$ .

The analytical approximations of  $\lambda_{||}$  for the RS model for protons is given by

$$\begin{aligned}\lambda_{||} &\propto \left(\frac{P}{P_0}\right)^2 \quad \text{for } P > 10^4 \text{ MV}, \\ \lambda_{||} &\propto \left(\frac{P}{P_0}\right)^{\frac{1}{3}} \quad \text{for } 10^{-1} \text{ MV} \leq P \leq 10^4 \text{ MV}, \\ \lambda_{||} &\propto \left(\frac{P}{P_0}\right) \quad \text{for } P < 10^{-1} \text{ MV}.\end{aligned}\tag{3.21}$$

Also the  $\lambda_{||}$  as given by RS model for electrons and positrons

$$\begin{aligned}\lambda_{||} &\propto \left(\frac{P}{P_0}\right)^2 \quad \text{for } P > 10^4 \text{ MV}, \\ \lambda_{||} &\propto \left[ \frac{2.27}{\sqrt{\left(\frac{P_e}{P_0}\right)^2 + \left(\frac{P}{P_0}\right)^2}} + 0.018 \left(\frac{P}{P_0}\right)^{\frac{1}{3}} \right] \quad \text{for } 10^{-1} \text{ MV} \leq P \leq 10^4 \text{ MV}, \\ \lambda_{||} &\propto \left(\frac{P}{P_0}\right) \quad \text{for } P < 10^{-1} \text{ MV}.\end{aligned}\tag{3.22}$$

The expression for  $\lambda_{||}$  as proposed by *Teufel and Schlickeiser (2002, 2003)* at Earth for protons (damping model) is used in this study and is valid for  $10^{-1} \text{ MV} \leq P \leq 10^4 \text{ MV}$  is  $\lambda_{||} \propto P^{\frac{1}{3}}$  (see Figure 3.8 top panel). Therefore, for the rigidity dependence it is assumed,

$$\lambda_{||} = C_1 \left(\frac{P}{P_0}\right)^{\frac{1}{3}}.\tag{3.23}$$



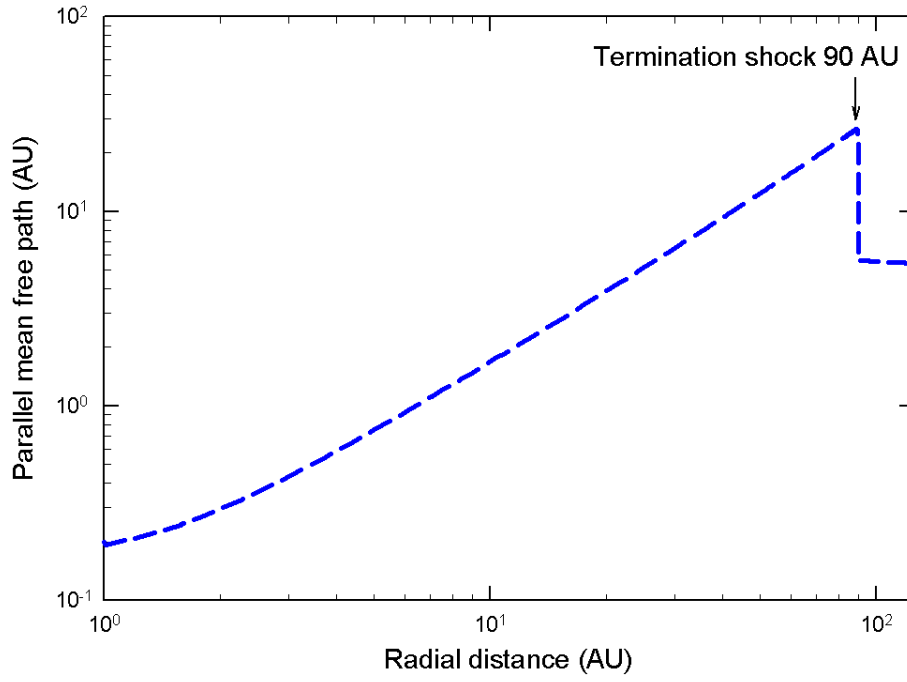


Figure 3.10: The parallel mean free path  $\lambda_{||}$  of *Burger et al. (2008)*; *Engelbrecht (2008)* as illustrated by *Strauss (2010)*, as a function of radial distance for 1 GV protons in the equatorial plane. The TS position is indicated by an arrow at 90 AU.

Here  $C_1$  is a constant in units of AU which determines the absolute value of the mean free path at Earth.

Figure 3.9 shows the proton parallel mean free path  $\lambda_{||}$ , at Earth as a function of rigidity using Equation 3.23 with  $C_1 = 0.6$  AU. Note that this value of  $C_1$  is for illustration purpose only and is changed later. Also a solar cycle (time) dependent function will be added later to this expression. The shaded box in the figure represents the Palmer consensus values.

### 3.5.2 Radial dependence

The  $\lambda_{||}$  used for this study is similar to that used by *Burger et al. (2008)*; *Engelbrecht (2008)*; *Strauss (2010)*. These authors used  $\lambda_{||}$  for protons (neglecting the dissipation range of turbulence spectrum) based on the results of *Teufel and Schlickeiser (2003)* giving

$$\lambda_{||} = \frac{3s}{\pi(s-1)} k_{min} R_L^2 \left( \frac{B}{\delta B_{slab,x}} \right)^2 \left( \frac{1}{4} + \frac{2(k_{min} R_L)^{-s}}{(2-s)(4-s)} \right) \quad (3.24)$$

with  $s = \frac{5}{3}$  the spectral index of the inertial range derived by Kolmogorov,  $R_L = \frac{P}{Bc}$  the Larmor radius and  $c$  the speed of light. The  $k_{min}$  by *Engelbrecht (2008)* is used in this study and is given as

$$k_{min} \propto \left( \frac{r}{r_0} \right)^{-0.4} \text{ m}^{-1} \quad \text{for } r \leq r_{ts}, \quad (3.25)$$

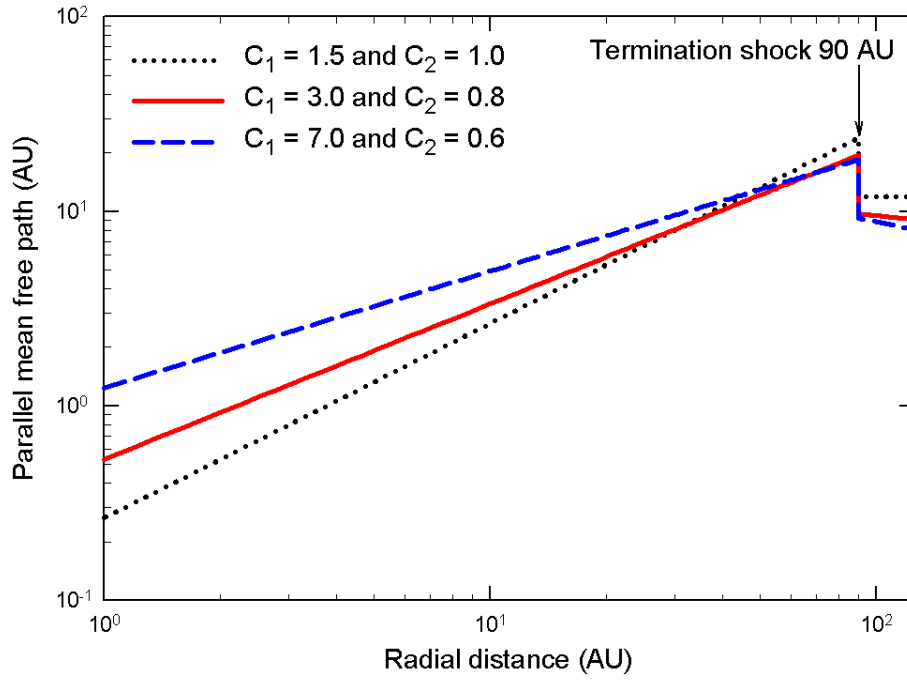


Figure 3.11: The parallel mean free path  $\lambda_{||}$ , as a function of radial distance for 1 GV protons in the equatorial plane. Three scenarios of  $\lambda_{||}$  in Equation 3.27 is shown namely:  $C_1 = 1.5$  and  $C_2 = 1.0$ ,  $C_1 = 3.0$  and  $C_2 = 0.8$  and  $C_1 = 7.0$  and  $C_2 = 0.6$  as indicated. The TS position is indicated by an arrow at 90 AU. Note that the value of the TS position and the absolute value of these coefficients are varied over a solar cycle later on.

where  $r_o = 1$  AU and  $r_{ts}$  is the TS position. This  $k_{min}$  is similar as given by [Burger et al. \(2008\)](#); [Strauss \(2010\)](#). In the heliosheath  $k_{min}$  is unknown, and therefore [Strauss \(2010\)](#) assumed it as a constant. In this work, this will also be the case.

The slab component of variance is assumed as ([Burger et al., 2008](#); [Strauss, 2010](#))

$$\delta B_{slab,x}^2 = 13.2 \left( \frac{r_0}{r} \right)^{2.5} \text{ nT}^2 \quad \text{for } r < r_{ts}. \quad (3.26)$$

Also the slab component of variance is unclear in the heliosheath and it is assumed in this region that,  $\delta B_{slab,x}^2 \sim B^2$ .

Figure 3.10 shows the  $\lambda_{||}$  from [Strauss \(2010\)](#) as a function of radial distance for 1 GV protons in the equatorial plane with  $\lambda_{||} \propto r^{\sim 1.2}$  for larger radial distance ( $r > 5$  AU) inside the  $r_{ts}$ , which is located at 90 AU. Across the  $r_{ts}$ ,  $\lambda_{||}$  drops as  $s_k^2$  and then decreases as  $\lambda_{||} \propto r^{-1}$ , where  $s_k = 2.5$ , the compression ratio assumed by [Strauss \(2010\)](#).

In this work it is therefore assumed that

$$\lambda_{||} = C_1 \left( \frac{P}{P_0} \right)^{\frac{1}{3}} \left( \frac{r}{r_0} \right)^{C_2} \quad \text{for } r < r_{ts}. \quad (3.27)$$

Here  $C_2$  is a dimensionless constant determining the radial dependence resulting in a similar radial dependence as used by e.g. [Strauss \(2010\)](#); [Manuel et al. \(2011a\)](#). In Chapter 6 a modification to this is proposed which includes a time-dependence.

Figure 3.11 shows the  $\lambda_{||}$  as a function of radial distance for 1 GV protons in the equatorial plane. Shown are three different scenarios each with different radial dependence determined by the value of  $C_2$  and magnitude by  $C_1$ . Three scenarios (different  $C_1$  and  $C_2$  as will be used in the following chapters) are shown as dashed, solid and dotted lines in the figure respectively. The  $C_1$  value determines the magnitude of  $\lambda_{||}$  and  $C_2$  the radial dependence *i.e.*  $\lambda_{||} \propto r^{C_2}$ . Figure 3.11 also shows that  $\lambda_{||}$  is smaller at Earth for  $C_1 = 1.5$  and  $C_2 = 1.0$  when compared to the other two scenarios. However, in the outer heliosphere for  $C_1 = 1.5$  and  $C_2 = 1.0$ ,  $\lambda_{||}$  becomes larger compared to the other two scenarios.

The TS position in Figure 3.11 is represented by an arrow (in this case at 90 AU) and here the  $\lambda_{||}$  is decreased by a factor  $s_k = 2$  (Richardson *et al.*, 2008), and then further decreases as  $r^{-1}$  (see Manuel *et al.*, 2011a,c) up to the heliopause. This is in accordance with Voyager observations of  $B$  which indicates that  $B \propto r$  (Burlaga *et al.*, 2007) for  $r > r_{ts}$ . Similar assumptions for the diffusion parameters were made previously by e.g. Florinski *et al.* (2003), Ferreira and Scherer (2006), Ferreira *et al.* (2007a), Ferreira *et al.* (2007b) and Strauss *et al.* (2010a) in order to compute realistic anomalous and galactic cosmic ray intensities. These authors assumed that the transport coefficients are roughly inversely proportional to the HMF magnitude  $B$ . This field increases suddenly over the TS and then increases toward the heliopause due to flow deceleration. Therefore, in this region

$$\lambda_{||} = \frac{C_1}{s_k} \left( \frac{P}{P_0} \right)^{\frac{1}{3}} \left( \frac{r}{r_0} \right)^{C_2} \left( \frac{r_{ts}}{r} \right) \quad \text{for } r \geq r_{ts}. \quad (3.28)$$

Note that the position of the shock is not necessarily stationary in this model. This will be discussed in more detail in the following chapters.

### 3.6 Perpendicular diffusion coefficient

The perpendicular diffusion coefficient  $K_{\perp}$  describe the diffusion perpendicular to the average HMF. The perpendicular particle scatterings are mainly as a result of the gyrocentres of the particles being displaced transverse to the mean magnetic field due to the fluctuations or the random walk of the magnetic field lines (Jokipii, 1966; Minnie *et al.*, 2009). Furthermore in 2D,  $K_{\perp r}$  is defined as the perpendicular diffusion coefficient in the radial direction and  $K_{\perp \theta}$  is defined as the perpendicular diffusion coefficient in the polar direction respectively.

Due to the complexity of perpendicular diffusion theoretical work on this coefficient progressed slowly. However, to solve the problem of cosmic ray diffusion across the mean magnetic field, different approaches have been developed by various authors (e.g. Jokipii, 1966; Kota and Jokipii, 2000; Matthaeus *et al.*, 2003; Shalchi *et al.*, 2004; Webb *et al.*, 2006). Quasilinear theory (QLT) by Jokipii (1966), where a slab turbulence geometry was assumed, is considered as the first theoretical description of parallel and perpendicular transport of charged particles. The QLT described perpendicular transport via the Field Line Random Walk (FLRW) limit which

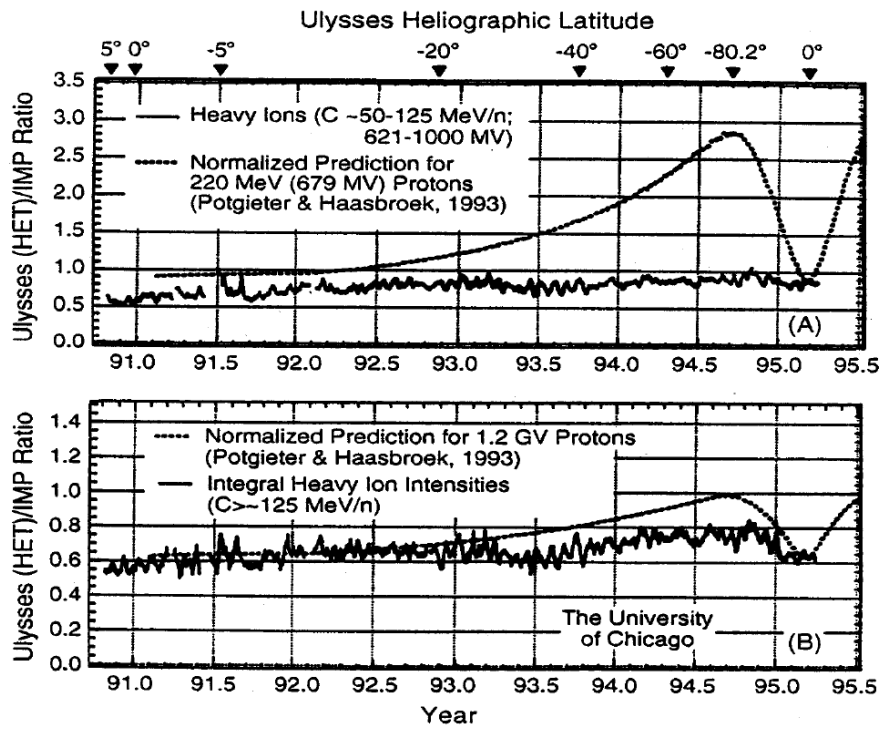


Figure 3.12: The ratio of Ulysses cosmic ray observations to IMP observations (solid line) is compared with a classical drift model (dotted line) by *Potgieter and Haasbroek (1993)*. The observed cosmic ray ratio between the two spacecraft is shown as a function of time and latitude (top). In this time interval Ulysses left the equatorial plane and returned after passing the Sun around the South Pole. The two panels represent observations and model results at different rigidities with the higher rigidity (1.2 GV) in the lower panel and the lower rigidity (679 MV) in the top panel. From *Smith (2000)*.

predicted a diffusive behaviour while computer simulations of test particles (e.g. *Qin et al., 2002a,b; Minnie et al., 2009*) discovered subdiffusion, implying that the QLT is not appropriate for perpendicular transport. This approach neglected pitch angle scattering, and as a result, failed to explain perpendicular transport of low energy particles. Also, this approach was doubtful while considering particle transport in nonslab models such as slab/2D composite model turbulence geometry.

A new approach which seems to agree with simulations was developed by *Matthaeus et al. (2003)* called the NonLinear Guiding Centre (NLGC) theory, which describes perpendicular diffusion in non-slab models. This approach assumed that the velocity of the particle gyrocentres that follow magnetic field lines determines the perpendicular particle transport and the magnetic field lines undergo diffusive separation (*Matthaeus et al., 2003*). However, for slab turbulence the NLGC theory provides a diffusive result which disagrees with the numerical results (see *Shalchi, 2009*, for a review). Later, several authors suggested different approaches to improve this theory (e.g. *Shalchi et al., 2004; Shalchi, 2005a; Stawicki, 2005b; Shalchi, 2006; Qin, 2007; Dosch et al., 2009; Le Roux et al., 2010; Shalchi, 2010*). Due to the complexity of these theories, a more simpler approach is used for this study, which is discussed below.

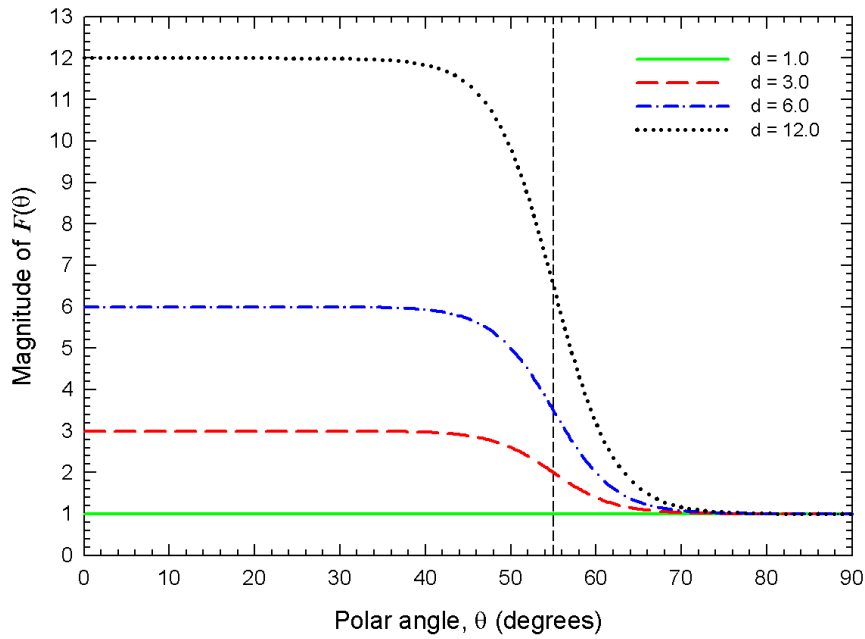


Figure 3.13: The function  $F(\theta)$  given by Equation 3.32 as a function of polar angle for four different values of  $d$ . The vertical dashed line represents the polar angle  $\theta = 55^\circ$  where  $F(\theta) = \frac{d+1}{2}$ .

The importance of  $K_\perp$ , especially for low energies, was reported by e.g. *Potgieter and Ferreira (1999)* and *Ferreira et al. (2000)* who studied galactic electron modulation in the heliosphere. As a first-order approach it has been standard practice by different authors using modulation models to scale  $K_\perp$  with  $K_\parallel$ , e.g.  $K_\perp \propto K_\parallel$  (see *Potgieter and Haasbroek, 1993*; *Jokipii et al., 1995*; *Le Roux et al., 1996*; *Giacalone, 1998*; *Hattingh, 1998*; *Burger et al., 2000*; *Ferreira et al., 2000*; *Strauss, 2010*).

Before the Ulysses spacecraft mission, which explored higher heliographic latitudes, it was commonly believed that a significant latitudinal gradient existed in cosmic ray proton intensities in the heliosphere during the A>0 polarity cycle. The reason behind this belief was that the cosmic ray protons mostly enter the heliosphere through polar regions during an A>0 HMF polarity cycle. This was proved not to be the case when Ulysses observations showed that the latitudinal gradients are not that significant as predicted by classic drift models (e.g. *Potgieter and Haasbroek, 1993*; *Haasbroek et al., 1995*; *Heber et al., 1996*).

Figure 3.12 shows the ratio between the observations from the Ulysses and IMP 8 spacecraft compared to the prediction by a classical drift modulation model by *Potgieter and Haasbroek (1993)*. This ratio shows the extent of the latitudinal gradients in the heliosphere as Ulysses went to higher latitudes compared to IMP 8, which stayed in the equatorial regions. The time interval shown in the figure represents the time Ulysses left the equatorial plane near Jupiter's orbit and moved towards the South Pole of the Sun, then executing a fast latitude scan from the South Pole to the North Pole.

The top and bottom panels in Figure 3.12 also show the model results (dotted lines) of *Potgieter and Haasbroek (1993)* compared to the observations (solid lines) for different proton rigidities, with lower rigidity (679 MV) in the top panel and higher rigidity (1.2 GV) in the bottom panel. The top panel shows that, for lower rigidity protons, the classical drift models predicted a significant increase in cosmic ray intensities from equator to the poles by as much as  $\sim 300\%$ . However, the observations only show a  $\sim 25\text{-}30\%$  increase. For higher rigidities, shown in the lower panel of the figure. The observations showed a  $\sim 15\text{-}20\%$  increase between the equatorial and polar regions, while the model predicted a  $\sim 150\%$  increase. These Ulysses observations showed that the latitudinal gradients in the inner heliosphere were much smaller than initially thought, suggesting amongst other reasons, a larger  $K_{\perp}$  towards the poles to be assumed in the modulation models in order to compute compatible results when compared to observations.

A new concept of  $K_{\perp}$  was formed in which this coefficient could be anisotropic and that  $K_{\perp}$  is larger towards the polar direction than the radial direction (see e.g. *Kota and Jokipii, 1995; Potgieter, 1996; Kota and Jokipii, 1997; Potgieter, 1997; Potgieter et al., 1997*). *Potgieter (1997)* and *Potgieter et al. (1997)* showed that assuming an anisotropic  $K_{\perp}$  meaning  $K_{\perp r} \neq K_{\perp \theta}$  and increasing  $K_{\perp \theta}$  towards the polar direction leads to a significant increase in the radial dependence in cosmic ray intensities, which has to be compensated for by reducing the drifts in order to produce a realistic computed result compatible with the observations both in latitude and radial distance.

Concerning modulation studies (e.g. *Jokipii and Kota, 1995; Jokipii et al., 1995; Potgieter, 1996; Burger et al., 2000; Ferreira, 2002; Moeketsi et al., 2005; Ndiitwani, 2005; Strauss, 2010; Manuel et al., 2011a,c; Ngobeni and Potgieter, 2011*), it has become standard practice to assume  $K_{\perp \theta} > K_{\perp r}$  to attain more realistic latitudinal gradients for cosmic ray intensity computations. It was also shown via simulations that both  $K_{\perp r}$  and  $K_{\perp \theta}$  can be scaled as the  $K_{\parallel}$  (*Le Roux et al., 1999; Giacalone and Jokipii, 1999; Qin et al., 2002a*) i.e.  $K_{\perp} \propto K_{\parallel}$ , so for this study

$$K_{\perp r} = aK_{\parallel} \quad (3.29)$$

and

$$K_{\perp \theta} = bK_{\parallel} \quad (3.30)$$

where  $a$  and  $b$  are either dimensionless constants or functions of rigidity (see *Burger et al., 2000; Ferreira, 2002; Ndiitwani, 2005; Manuel et al., 2011c*). These constants will be more thoroughly discussed later.

In this study, in order to reproduce the observed Ulysses cosmic ray intensity gradients, an enhanced latitudinal transport as suggested by *Burger et al. (2000)* is used i.e.  $K_{\perp \theta}$  increases towards the poles. This is done by introducing a function and a modified  $K_{\perp \theta}$  is assumed as

$$K_{\perp \theta} = bF(\theta)K_{\parallel}. \quad (3.31)$$

Here  $F(\theta)$  is a function enhancing  $K_{\perp \theta}$  towards the pole by a factor  $d$ , as suggested by *Burger*

*et al.* (2000), and is given by

$$F(\theta) = A^+ - A^- \tanh \left[ \frac{1}{\Delta\theta} (\theta - 90^\circ + \theta_F) \right], \quad (3.32)$$

where  $A^\pm = \frac{d \pm 1}{2}$ ,  $\Delta\theta = \frac{1}{8}$  and  $\theta_F = 35^\circ$ . Figure 3.13 shows the function  $F(\theta)$  (in one quadrant only) as a function of polar angle for different  $d$  values namely 1.0, 3.0, 6.0 and 12.0. The magnitude of  $F(\theta)$  increases from 1.0 at the equatorial plane towards the poles and reaches value  $d$  near the polar regions. The vertical dashed line represents the polar angle  $\theta = 55^\circ$  where  $F(\theta) = \frac{d+1}{2}$ .

Enhancing the cross-field diffusion in the polar direction using the function  $F(\theta)$  was motivated by *Burger et al.* (2000) using Ulysses observations during its fast latitude scan periods. These authors argued that the observations showed an increase in variance  $\delta B^2$  normal to the magnetic field lines than in the radial direction, which possibly indicated a more effective cross-field diffusion. Since for this study a Parker field is used, an enhanced  $K_{\perp\theta}$  is achieved by introducing the function  $F(\theta)$  (see also *Ferreira and Potgieter, 2004; Ngobeni and Potgieter, 2010*). A discussion on Fisk field (*Fisk, 1996*) is presented in Chapter 2. Such a HMF with a meridional component may also lead to more effective perpendicular diffusion (*Burger and Hattingh, 2001; Burger and Hitge, 2004; Sternal et al., 2011*). Furthermore, *Ngobeni and Potgieter (2011)* introduced an asymmetry in how  $K_{\perp\theta}$  depends on polar angle.

In addition, *Ferreira et al. (2003a,b)* and *Moeketsi et al. (2005)* pointed out the need for a time-dependence in this function to fully describe low-energy electron modulation during moderate to extreme solar maximum conditions. *Moeketsi et al. (2005)* proposed to relate the function  $F(\theta)$  to the latitudinal dependence of the solar wind speed. *Ferreira et al. (2003a,b)* investigated the effect of different  $d$  dependence on 7 MeV electron intensities along the Ulysses spacecraft trajectory. When compared to 3–10 MeV electrons observations by the KET instrument on-board the Ulysses spacecraft (*Heber et al., 2002*), they found that varying  $d$  over a solar cycle resulted in improved compatibility between model results and low energy electron observations.

### 3.7 Drift coefficient

Cosmic ray particles drift in and out of the heliosphere under the influence of gradient and curvatures in the HMF and the HCS. However, the importance of drift was neglected in initial modulation model studies until *Jokipii et al. (1977)* pointed out its significance. *Jokipii et al. (1977)* reported that, even though gradient and curvature drifts have been incorporated into the formal theory of cosmic ray transport as studied by e.g. *Parker (1965); Gleeson and Axford (1967); Jokipii and Parker (1970)*, most modulation models neglected drifts in the heliosphere. *Jokipii et al. (1977)*, using a Parker HMF, showed that the particle drifts contribute substantially to cosmic ray transport. Later, the importance of drift was confirmed by models incorporating drift effects (e.g. *Jokipii and Davila, 1981; Potgieter and Moraal, 1985*).



In a heliosphere with an assumed background Parker spiral HMF, cosmic ray particles undergo drifts due to physical phenomena such as gradients in the magnetic field, curvature of the field lines and any abrupt changes in the field direction, such as that at the HCS, where a sudden switch in HMF polarity occurs across the HCS. These drift processes are embedded in the TPE as given by Equation 3.1 or 3.2.

For clarity, the TPE in a 3D spherical coordinate system as given in Equation 3.2 can be rewritten to highlight the different drift velocities and showing each process namely diffusion, drift, convection and adiabatic energy changes (in this work only energy changes due to adiabatic cooling is considered) as,

$$\begin{aligned}
 \frac{\partial f}{\partial t} = & \overbrace{\left[ \frac{1}{r^2} \frac{\partial}{\partial r} (r^2 K_{rr}) + \frac{1}{r \sin \theta} \frac{\partial K_{\phi r}}{\partial \phi} \right] \frac{\partial f}{\partial r} + \left[ \frac{1}{r^2 \sin \theta} \frac{\partial}{\partial \theta} (K_{\theta \theta} \sin \theta) \right] \frac{\partial f}{\partial \theta}}^{\text{diffusion}} \\
 & + \overbrace{\left[ \frac{1}{r^2 \sin \theta} \frac{\partial}{\partial r} (r K_{r\phi}) + \frac{1}{r^2 \sin^2 \theta} \frac{\partial K_{\phi \phi}}{\partial \phi} + \Omega \right] \frac{\partial f}{\partial \phi}}^{\text{diffusion}} \\
 & + \overbrace{K_{rr} \frac{\partial^2 f}{\partial r^2} + \frac{K_{\theta \theta}}{r^2} \frac{\partial^2 f}{\partial \theta^2} + \frac{K_{\phi \phi}}{r^2 \sin^2 \theta} \frac{\partial^2 f}{\partial \phi^2} + \frac{2K_{r\phi}}{r \sin \theta} \frac{\partial^2 f}{\partial r \partial \phi}}^{\text{diffusion}} \\
 & + \overbrace{\left[ -\langle \mathbf{v}_d \rangle_r \right] \frac{\partial f}{\partial r} + \left[ -\frac{1}{r} \langle \mathbf{v}_d \rangle_\theta \right] \frac{\partial f}{\partial \theta} + \left[ -\frac{1}{r \sin \theta} \langle \mathbf{v}_d \rangle_\phi \right] \frac{\partial f}{\partial \phi}}^{\text{drift}} \\
 & + \overbrace{-V \frac{\partial f}{\partial r}}^{\text{convection}} \\
 & + \overbrace{\frac{1}{3r^2} \frac{\partial}{\partial r} (r^2 V) \frac{\partial f}{\partial \ln P}}^{\text{adiabatic energy change}} \\
 & + \overbrace{Q}^{\text{sources}}.
 \end{aligned} \tag{3.33}$$

The first three lines of the above equation are the terms describing the inward diffusion of the particles, the fourth line describes the drift effects caused by the magnetic field, the fifth line the outward convection caused by the solar wind, the sixth line represents the adiabatic energy change and the last line represents any sources inside the heliosphere, and  $\Omega$  represents the angular speed of the Sun. The components of the gradient, curvature and current sheet drifts in Equation 3.33 are given as,

$$\begin{aligned}
 \langle \mathbf{v}_d \rangle_r &= -\frac{A^*}{r \sin \theta} \frac{\partial}{\partial \theta} (K_{\theta r} \sin \theta) \mathbf{e}_r, \\
 \langle \mathbf{v}_d \rangle_\theta &= -\frac{A^*}{r} \left( \frac{\partial}{\partial r} (r K_{r\theta}) + \frac{1}{\sin \theta} \frac{\partial}{\partial \phi} (K_{\phi \theta}) \right) \mathbf{e}_\theta, \\
 \langle \mathbf{v}_d \rangle_\phi &= -\frac{A^*}{r} \frac{\partial}{\partial \theta} (K_{\theta \phi}) \mathbf{e}_\phi
 \end{aligned} \tag{3.34}$$



where,

$$A^* = \begin{cases} +1 & \text{if } qA > 0 \\ -1 & \text{if } qA < 0 \end{cases}$$

with  $q$  is the particle charge. Here  $A = \pm 1$  a constant denoting the polarity of the HMF which switches between a positive and a negative value  $\sim 11$  years, and is considered positive when HMF is directed outwards, and negative when directed inwards in the northern hemisphere of the Sun.

The average drift velocity of a nearly isotropic particle distribution is given by

$$\langle \mathbf{v}_d \rangle = \nabla \times K_A \mathbf{e}_B, \quad (3.35)$$

with  $\mathbf{e}_B = \frac{\mathbf{B}}{B}$  a unit vector in the direction of magnetic field  $\mathbf{B}$  and  $K_A$  the drift coefficient.

The average drift velocity in the Parker magnetic field follows from Equation 3.35 (see *Hattingh, 1998; Ferreira, 2002*) as,

$$\langle \mathbf{v}_d \rangle = \nabla \times K_A \mathbf{e}_B (1 - 2H(\theta - \theta')) + 2\delta_d(\theta - \theta') K_A \mathbf{e}_B \times \nabla(\theta - \theta'). \quad (3.36)$$

Here the first term represents the gradient and curvature drifts due to the Parker HMF and the second term represents the drift as a result of the HCS. The Heaviside step function is given as  $H$  (see Equation 2.15) and  $\theta$  the polar angle with  $\theta'$  the polar angle describing the position of the neutral sheet (HCS) and  $\delta_d$  the Dirac function given by,

$$\delta_d(\theta - \theta') = \begin{cases} 0 & \text{if } \theta \neq \theta' \\ \infty & \text{if } \theta = \theta'. \end{cases} \quad (3.37)$$

The Wavy Current Sheet<sup>1</sup> (WCS) model, as introduced by *Hattingh and Burger (1995b); Burger and Hattingh (1995); Hattingh (1998)* is used in this work to simulate the HCS in a 2D time-dependent modulation model. In this WCS-model the three-dimensional drift velocity is replaced by a two-dimensional drift velocity, which is obtained by averaging Equation 3.36 over one solar rotation and is given by,

$$\langle \mathbf{v}_d \rangle = g(\theta) \nabla \times K_A \frac{\mathbf{B}}{B} + \frac{2Prv\Gamma}{3cA\pi(1 + \Gamma^2) \left( (\alpha + \Delta\theta_{ns})^2 + \left( \frac{\pi}{2} - \theta \right)^2 \right)^{\frac{1}{2}}} \mathbf{e}_r. \quad (3.38)$$

The above expression is divergence free and is difficult to solve numerically, so an approximation is derived by these authors in such a way that it remains nearly divergence free and is given as,

$$\langle \mathbf{v}_d \rangle \approx g(\theta) \nabla \times K_A \frac{\mathbf{B}}{B} + \frac{Prv\Gamma'}{3cA(1 + \Gamma'^2)(\alpha + \Delta\theta_{ns})} \mathbf{e}_r \quad (3.39)$$

---

<sup>1</sup>Originally called Wavy Neutral Sheet (WNS) model.

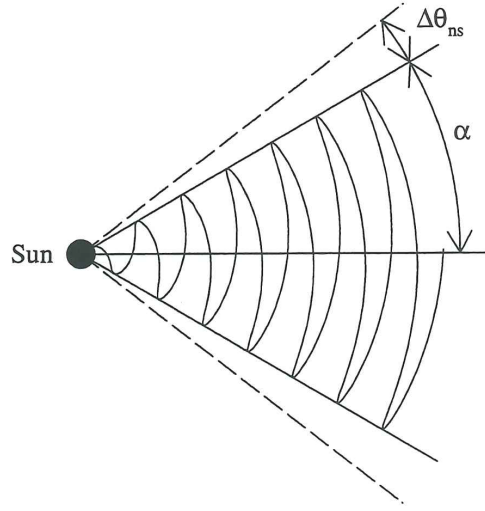


Figure 3.14: The HCS region for a tilt angle of  $\alpha = 30^\circ$ . From *Hattingh (1998)*.

with

$$g(\theta) = \begin{cases} 1, & \text{if } 0 \leq \theta \leq \frac{\pi}{2} - \alpha - \Delta\theta_{ns}, \\ \frac{2}{\pi} \sin^{-1} \left( \frac{\frac{\pi}{2} - \theta}{\alpha + \Delta\theta_{ns}} \right), & \text{if } \frac{\pi}{2} - \alpha - \Delta\theta_{ns} < \theta < \frac{\pi}{2} + \alpha + \Delta\theta_{ns}, \\ -1, & \text{if } \frac{\pi}{2} + \alpha + \Delta\theta_{ns} \leq \theta \leq \pi \end{cases} \quad (3.40)$$

where  $r$  the radial distance from the Sun,  $\Omega$  the angular speed of the Sun,  $V$  the magnitude of radial solar wind velocity,  $\alpha$  the tilt angle,  $\Delta\theta_{ns} = \frac{2R_L}{r}$  the angle spanned by two gyroradii (Larmor radii),  $R_L = \frac{P}{Bc}$  the Larmor radius,  $v$  the particle speed,  $P$  rigidity,  $c$  the speed of light,  $\Gamma = \tan \psi = \frac{\Omega(r - r_\odot)}{V}$ ,  $\psi$  the spiral angle,  $\Gamma' = \frac{\Omega(r - r_\odot)}{V} \cos \left( \frac{\alpha}{\sqrt{2}} \right)$  and  $r_\odot$  the radius of the Sun.

Equation 3.38 represents the sum of the curvature and the gradient drift  $\langle \mathbf{v}_d^* \rangle$  and the HCS drift  $\langle \mathbf{v}_d^{ns} \rangle$ , i.e.

$$\langle \mathbf{v}_d \rangle = \langle \mathbf{v}_d^* \rangle + \langle \mathbf{v}_d^{ns} \rangle. \quad (3.41)$$

The first term of Equation 3.38 represents the curvature and gradient drift and is given by,

$$\langle \mathbf{v}_d^* \rangle = g(\theta) \nabla \times K_A \frac{\mathbf{B}}{B}. \quad (3.42)$$

The function  $g(\theta)$  has the effect of scaling the curvature and gradient drift down over the HCS region so that it is zero at  $\theta = \frac{\pi}{2}$ .

The HCS drift is represented by the second term of Equation 3.38,

$$\langle \mathbf{v}_d^{ns} \rangle = \frac{Prv\Gamma'}{3cA(1 + \Gamma'^2)(\alpha + \Delta\theta_{ns})} \mathbf{e}_r. \quad (3.43)$$

The HCS drift outside the HCS regions  $0 \leq \theta \leq \frac{\pi}{2} - \alpha - \Delta\theta_{ns}$  and  $\frac{\pi}{2} + \alpha + \Delta\theta_{ns} \leq \theta \leq \pi$  where  $g(\theta) = \pm 1$  is zero. The HCS region  $\frac{\pi}{2} - \alpha - \Delta\theta_{ns} < \theta < \frac{\pi}{2} + \alpha + \Delta\theta_{ns}$  is defined as the region

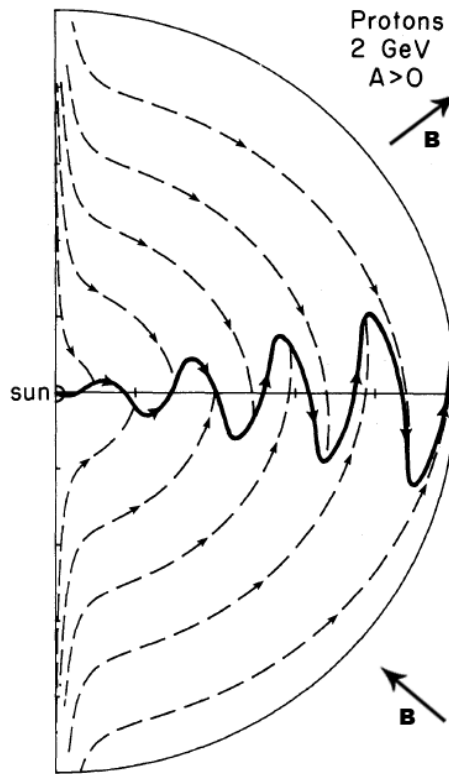


Figure 3.15: Meridional projection of drift trajectories for 2 GeV protons during an  $A > 0$  magnetic polarity cycle i.e. when the HMF is directed outward in the northern hemisphere and inwards in the southern hemisphere of Sun. The arrows will change to opposite direction during an  $A < 0$  HMF polarity cycle or when electron drifts are considered. From *Jokipii and Thomas (1981)*.

swept out by particles drifting along the HCS during one solar rotation. In this way the effect of the HCS is simulated by the WCS-model. A graphical representation of the HCS region for a tilt angle of  $\alpha = 30^\circ$  is shown in Figure 3.14.

Figure 3.15 shows a graphical representation showing a meridional projection of gradient, curvature and current sheet drift velocity directions for 2 GeV protons during an  $A > 0$  magnetic polarity cycle. The HMF polarity cycle is  $A > 0$  when the HMF is directed outward in the northern hemisphere and inwards in the southern hemisphere of the Sun and it is considered as  $A < 0$  HMF polarity cycle when the HMF switches its direction in the northern hemisphere inward and the southern hemisphere outwards. During an  $A > 0$  HMF polarity cycle, positively charged particles (protons) drift into the heliosphere, primarily from the polar regions down onto the equatorial regions and outwards along the HCS. The wavy curve in Figure 3.15 represents the drift along the HCS which dominates the equatorial motion. However, during an  $A < 0$  HMF polarity cycle positively charged particles drift in along the HCS towards the Sun and exit through the polar regions. i.e. the arrows in the Figure 3.15 change to opposite direction during an  $A < 0$  HMF polarity cycle or when negatively charged particle (electron) drifts are considered.

Under the assumption of weak scattering, the drift coefficient  $K_A$  in Equation 3.35 and 3.36

as given by the standard approach (*Forman et al., 1974; Jokipii and Kopriva, 1979; Potgieter, 1984; Burger and Potgieter, 1989*) is,

$$K_A = K_{A0} \frac{\beta P}{3B} \quad (3.44)$$

where  $\beta = \frac{v}{c}$ , the ratio of the particle speed to the speed of light,  $B$  is the modified HMF magnitude (*Jokipii and Kota, 1989*) where the mean field magnitude is increased compared to a pure Parker type field in the heliospheric polar regions and  $K_{A0}$  is a dimensionless constant which scale  $K_A$  and has a value from 0 to 1 representing zero drift to full drift (*Potgieter and Le Roux, 1989*).

The drift coefficient used in this work is from *Burger et al. (2000, 2008)* and is given by

$$K_A = K_{A0} \frac{\beta P}{3B} \frac{\left(\frac{P}{P^*}\right)^2}{\left[\left(\frac{P}{P^*}\right)^2 + 1\right]} \quad (3.45)$$

where  $P^* = \frac{1}{\sqrt{10}} \text{GV}$ .

This modified approach results in a decrease of  $K_A$  for  $P < 600 \text{ MV}$  which is steeper compared to the standard approach as given in Equation 3.44. A justification for this modification is based on calculations of the rigidity dependence for proton latitudinal gradients and comparisons with major Ulysses observations (*Burger et al., 2000*). The fact that drift is reduced by the presence of turbulence has been established by direct numerical simulations (e.g. *Giagalone et al., 1999; Minnie et al., 2007*). This choice of modified drift coefficient is consistent with the numerical simulations of *Giagalone et al. (1999)* as well as the observational results of *Lockwood and Webber (1992)*. The reduction at low rigidity is also in agreement with the results of *Webber et al. (1990)*.

### 3.8 Example steady-state solutions

Figure 3.16 shows example model solutions depicting the effects of different  $K_{\perp r}$  (different  $a$  value as given in Equation 3.29), the effects of different  $K_{\perp \theta}$  (different  $b$  value as given in Equation 3.31) and also the effects of different  $d$  values, as given in Equation 3.31, on computed 2.5 GV cosmic ray radial profiles during an  $A < 0$  polarity cycle. During an  $A < 0$  polarity cycle, the protons drift in along the HCS towards the Sun and depart through the polar regions. A 2D steady-state transport model with an assumed tilt angle of  $10^\circ$  is utilised to compute the intensities. The purpose of these figures is to show how these parameters influence the cosmic ray distribution in the heliosphere. A steady-state model is used to remove time-dependent effects and to focus on the sensitivity of the spatial distribution of cosmic rays on these parameters.

The 2.5 GV proton differential intensity as a function of radial distance is shown in the top left panel, Figure 3.16(a), which is regarded as a reference scenario showing the computed intensities with parameters  $a = 0.01$ ,  $b = 0.01$  and  $d = 6.0$ . Computed intensities for different polar

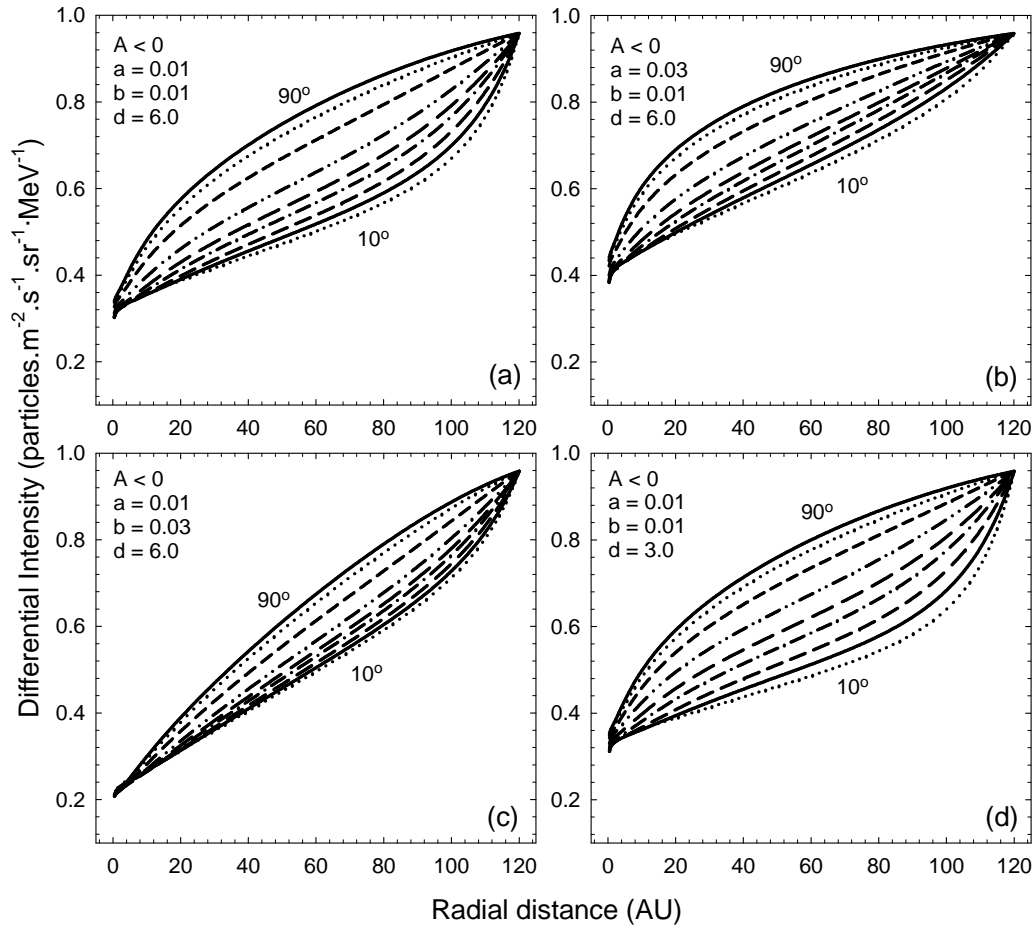


Figure 3.16: Computed 2.5 GV proton differential intensity as a function of radial distance for the  $A < 0$  polarity cycle. (a) Top left panel shows the reference scenario of computed intensities when  $a = 0.01$ ,  $b = 0.01$  and  $d = 6.0$  is assumed. (b) Top right panel shows the computed intensities when the  $a$  value is changed to  $a = 0.03$  while keeping  $b$  and  $d$  the same as for the reference scenario. (c) Bottom left panel shows the computed intensities when the value of  $b$  is changed from  $b = 0.01$  to  $b = 0.03$  while keeping  $a$  and  $d$  the same as for the reference scenario and (d) bottom right panel shows the computed intensities when the value of  $d$  is changed from  $d = 6.0$  to  $d = 3.0$  while keeping  $a$  and  $b$  the same as for the reference scenario. Also shown in all panels are the computed intensities for different polar angles in steps of  $10^\circ$  with  $90^\circ$  the equatorial plane (top line) and  $10^\circ$  the near polar region (bottom line).

angles from  $10^\circ$  near polar regions (bottom line) to  $90^\circ$  equatorial plane (top line) are shown in steps of  $10^\circ$ . Note that the idea is not to fit any data but just to show the sensitivity of the computed intensities to different  $a$ ,  $b$  and  $d$  values. The top right panel, Figure 3.16(b), shows the same as in the reference scenario Figure 3.16(a) except that the  $a$  value is changed to  $a = 0.03$  while keeping  $b$  and  $d$  the same. By comparing these two figures it follows that an increase in  $a$  leads to increase in cosmic ray intensities throughout the heliosphere. The computed radial gradient in the outer heliosphere (e.g.  $r \geq \sim 80$  AU) is decreased while the computed radial gradient in the inner heliosphere ( $r < \sim 80$  AU) is increased. Also, the latitudinal gradient in the outer heliosphere is significantly reduced by an increase in  $a$  value because less modulation

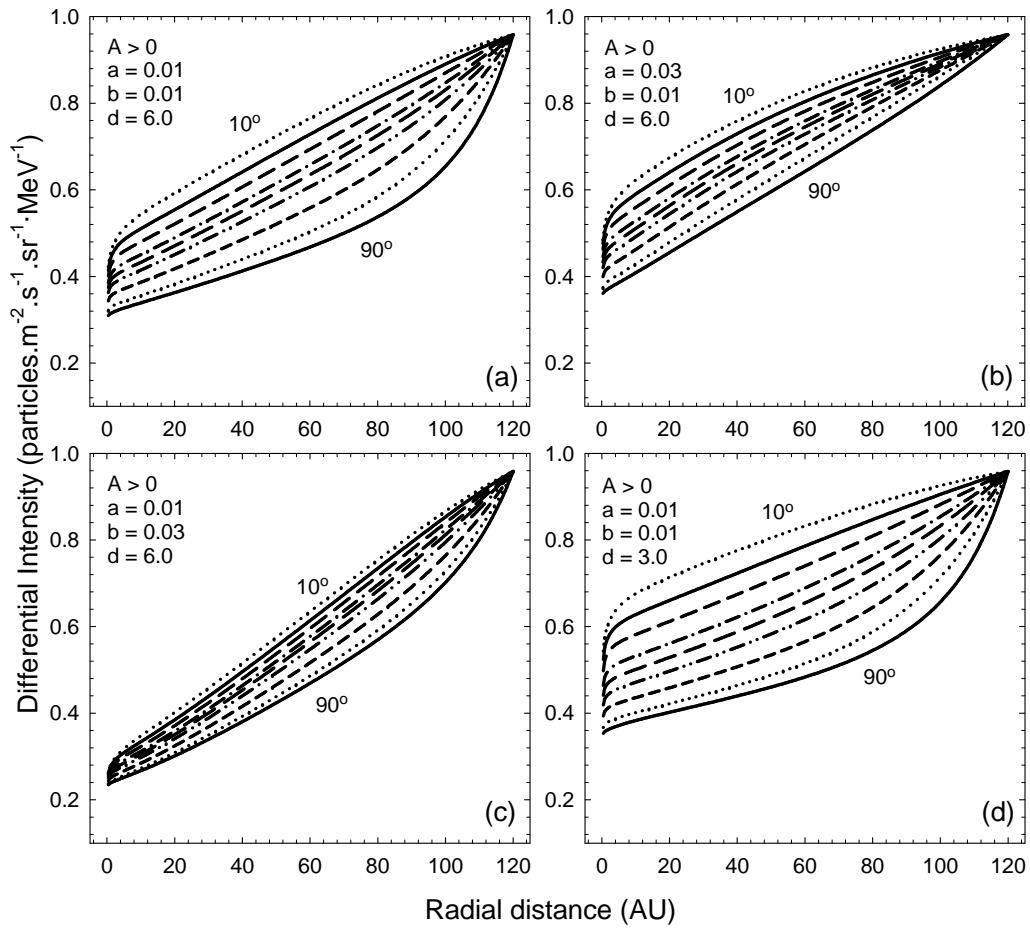


Figure 3.17: Same as in Figure 3.16 but for the  $A > 0$  polarity cycle. Also shown on all panels are computed intensities for different polar angles in steps of  $10^\circ$  with  $90^\circ$  the equatorial plane (bottom line) and  $10^\circ$  the near polar region (top line).

occurs.

Figure 3.16(c) shows the same as in reference scenario (a) but now with an increase in  $b$  value to  $b = 0.03$ , while keeping all other parameters same as in (a). Figure 3.16(c) shows that an increase in  $b$  value from 0.01 to 0.03 results in a decrease in the cosmic ray intensities in the inner heliosphere ( $r < \sim 80$  AU) and it also leads to an increase in the radial dependence of cosmic ray intensities in the outer heliosphere,  $r \geq \sim 80$  AU. The result is a decrease in the radial dependence for distances with a larger radial dependence and an increase in radial dependence for distances with a smaller radial dependence. Also an increase in the  $b$  value decreased the latitudinal dependence in the cosmic ray intensities (see [Potgieter, 1997](#); [Potgieter et al., 1997](#); [Ferreira, 2002](#)). Figure 3.16(d) shows the effect of a reduced  $d$  value. Here the enhancement towards the poles is reduced from 6.0 to 3.0, when compared to reference scenario (a). This in-turn increased the latitudinal gradient inside the heliosphere. For a decreased  $d$  value, an increase in latitudinal gradient towards the polar regions is computed.

Figure 3.17 shows same as in Figure 3.16 but for an  $A > 0$  polarity cycle. During this polarity cycle, protons drift in from the polar regions towards the Sun and exit along the HCS. The computed intensities for different polar angles from  $10^\circ$  near polar regions (top line) to  $90^\circ$  equatorial plane (bottom line) are shown in steps of  $10^\circ$ . Figure 3.17(a) is again considered as the reference scenario with  $a = 0.01$ ,  $b = 0.01$  and  $d = 6.0$ .

For an increased  $a$  value given by scenario in Figure 3.17(b), the computed cosmic ray intensities increase in the whole heliosphere. The radial gradient in the outer heliosphere,  $r \geq \sim 80$  AU is decreased but increased in the inner heliosphere,  $r < \sim 80$  AU. This figure also shows a more pronounced effect in the equatorial regions compared to the polar regions. Also the latitudinal gradient in the outer heliosphere is significantly reduced by an increase in the value of  $a$ , similar to Figure 3.16(b). Figure 3.17(c) (bottom left panel) shows a scenario with an increased  $b$  value from 0.01 as in Figure 3.17(a) to 0.03. The cosmic ray intensities in the whole heliosphere is decreased by an increased  $b$  value. However, the radial gradient increases for distances which have previously had a relatively smaller radial gradient (i.e. as in reference scenario (a) with  $b = 0.01$ ) and the radial gradient decreases for distances which previously had a relatively larger radial gradient *Ferreira (2002)*. Scenario (c) also shows an overall decrease in latitudinal gradient when compared to the reference scenario (a). Figure 3.17(d) shown in the bottom right panel shows computations with  $d = 3.0$  and is compared to  $d = 6.0$  in Figure 3.17(a). Here a decrease in  $d$  value increases the latitudinal gradient significantly in the inner heliosphere and moderately in the outer heliosphere. Also, the latitudinal gradient increases towards the polar regions for a smaller  $d$  value when compared to the reference scenario (a).

### 3.9 Summary

In this chapter, an overview of the Parker transport equation, which contains all the major modulation processes namely convection, energy changes, diffusion and drift were discussed. The diffusion tensor  $\mathbf{K}$  in a HMF aligned coordinate system was elaborated on distinguishing between a symmetric diffusion tensor  $\mathbf{K}_s$  and a asymmetric drift tensor  $\mathbf{K}_A$ . The symmetric diffusion tensor  $\mathbf{K}_s$  describes the cosmic ray diffusion along and perpendicular to the average HMF i.e. the parallel diffusion coefficient  $K_{||}$  is responsible for cosmic ray diffusion along the average HMF, perpendicular diffusion coefficient  $K_{\perp\theta}$  for diffusion perpendicular to the average HMF in  $\theta$  (polar) direction and perpendicular diffusion coefficient  $K_{\perp r}$  for diffusion perpendicular to the average HMF in  $r$  (radial) direction respectively. The asymmetric drift tensor  $\mathbf{K}_A$ , contains the drift coefficient  $K_A$  which represents gradient, curvature and current sheet drifts. The transformation of diffusion tensor from field aligned coordinate system to a spherical coordinate system was shown for the 2D modulation model used in this work.

Before discussing the different transport coefficients, a brief background on turbulence was given. This includes a discussion on the turbulence power spectrum and the different turbulence geometry models, i.e. the slab or 1D turbulence, 2D turbulence and the composite (or



two-component) turbulence. The total energy in the magnetic field fluctuations known as the magnetic field variance  $\delta B^2$  from a slab and a 2D geometry are important for this study since the diffusion parameters depend on these variances, as will be discussed later in Chapter 6.

The parallel diffusion coefficient  $K_{\parallel}$  used in this work is based on the calculations of *Teufel and Schlickeiser* (2002, 2003) at Earth using the damping (DT) model (see Figure 3.8) which assumed a set of interplanetary parameters as suggested by *Bieber et al.* (1994). The analytical approximations by these authors (at 1 AU for protons) are assumed for the rigidity dependence of  $K_{\parallel}$ , as given in Equation 3.23 and was shown in Figure 3.9. The radial dependence is similar as used by *Burger et al.* (2008); *Engelbrecht* (2008) and *Strauss* (2010) and is given by Equation 3.27 for distances inside the TS. The constants  $C_1$  and  $C_2$  in Equation 3.27 determines the absolute value of parallel mean free path at Earth and the radial dependence. At the TS position  $K_{\parallel}$  is decreased by a factor  $s_k = 2$  (*Richardson et al.*, 2008) and then further decreases as  $r^{-1}$  inside the inner heliosheath as given by Equation 3.28 (see *Manuel et al.*, 2011a,c).

Due to the slow progress and complexity of perpendicular diffusion theory, it has been standard practice by different authors using modulation models to scale  $K_{\perp}$  with  $K_{\parallel}$  (see *Potgieter and Haasbroek*, 1993; *Jokipii et al.*, 1995; *Le Roux et al.*, 1996; *Giacalone*, 1998; *Hattingh*, 1998; *Burger et al.*, 2000; *Ferreira et al.*, 2000; *Strauss*, 2010), e.g.  $K_{\perp} \propto K_{\parallel}$ . It has also become standard practice to assume  $K_{\perp\theta} > K_{\perp r}$  to attain a more realistic latitudinal gradients for cosmic ray intensity computations (e.g. *Jokipii and Kota*, 1995; *Jokipii et al.*, 1995; *Potgieter*, 1996; *Burger et al.*, 2000; *Ferreira*, 2002; *Moeketsi et al.*, 2005; *Ndiitwani*, 2005; *Strauss*, 2010; *Manuel et al.*, 2011a,c). For this study  $K_{\perp\theta}$  and  $K_{\perp r}$  are scaled with  $K_{\parallel}$  as given in Equations 3.29 and 3.31. Also, in order to reproduce the observed Ulysses cosmic ray intensity gradients, an enhanced latitudinal transport, as suggested by *Burger et al.* (2000), is implemented by introducing a function as given in Equation 3.31.

In a heliosphere with assumed background Parker spiral magnetic field, the cosmic ray particles experience gradient, curvature and current sheet drift motions. These drift processes are also embedded in the Parker transport equation. To simulate the HCS in this 2D time-dependent modulation model, the WCS model proposed by *Hattingh and Burger* (1995b) is utilised. In this model, the 3D drift velocity is replaced by a 2D drift velocity by averaging drift velocity over one solar rotation and the result is then approximated, to remain nearly divergence free, in order to solve it numerically. The drift coefficient  $K_A$  used in this work is adapted from *Burger et al.* (2000, 2008) as given in Equation 3.45 which resulted in  $K_A$  decrease for  $P < 600$  MV as a function of decreasing rigidity much faster than  $K_A$  in a standard approach (*Forman et al.*, 1974; *Jokipii and Kopriva*, 1979; *Burger and Potgieter*, 1989). The fact that drift is reduced by the presence of turbulence has been established by direct numerical simulations (e.g. *Giacalone et al.*, 1999; *Minnie et al.*, 2007). The choice of diffusion coefficient by *Burger et al.* (2000, 2008) is consistent with the numerical simulations of *Giacalone et al.* (1999), the observational results of *Lockwood and Webber* (1992) and agree with the result of *Webber et al.* (1990) for the low rigidities.



Lastly steady-state example solutions of cosmic ray intensities were shown to illustrate the effect of different diffusion parameters on the distribution of cosmic rays in the heliosphere, i.e.  $a$ , the ratio of perpendicular diffusion coefficient in the radial direction to parallel diffusion coefficient,  $b$ , the ratio of perpendicular diffusion coefficient in the polar direction to parallel diffusion coefficient and  $d$ , the enhancement factor of  $K_{\perp\theta}$  towards the poles. By varying these, the effect on cosmic ray intensities were shown for  $A < 0$  and  $A > 0$  polarity cycles.

In the next chapter an overview of the numerical transport model used in this work is discussed.